

Ice and Supercooled Liquid Water Distributions over the Southern Ocean based on In Situ Observations and Climate Model Simulations

Ching An Yang¹, Minghui Diao¹, Andrew Gettelman², Kai Zhang³, and Jian Sun⁴

¹San Jose State University

²National Center for Atmospheric Research (UCAR)

³Pacific Northwest National Laboratory

⁴Pacific Northwest National Laboratory (DOE)

November 24, 2022

Abstract

An evaluation of three climate models is conducted using in situ airborne observations from the Southern Ocean Clouds, Radiation, Aerosol Transport Experimental Study (SOCRATES) campaign. The evaluation targets cloud phases, microphysical properties, thermodynamic conditions, and aerosol indirect effects at $-40^{\circ}\text{C} - 0^{\circ}\text{C}$. For cloud phase frequency distribution, the Community Atmosphere Model version 6 (CAM6) shows the most similar result to the observations, which allows more liquid-containing clouds below -10°C compared with its predecessor – CAM5. The Energy Exascale Earth System Model (E3SM) underestimates (overestimates) ice phase frequencies below (above) -20°C . Compared with 580-second averaged observations (i.e., 100 km horizontal scale), CAM6 and E3SM overestimate (underestimate) liquid (ice) water content (i.e., LWC and IWC), leading to lower a glaciation ratio when ice and liquid coexist. Thermodynamic conditions, specifically relative humidity (RH), is likely a key factor contributing to model cloud occurrence and cloud phase biases. Simulated in-cloud RH shows higher minimum values than observations, possibly restricting ice growth during sedimentation. As number concentrations of larger and smaller aerosols (> 500 nm and > 100 nm) increase, observations show increases in glaciation ratio, cloud fraction, LWC and liquid number concentration (Nliq) at -18°C to 0°C , and IWC and ice number concentration (Nice) at -35°C to 0°C . CAM6 and E3SM show slight increases of LWC and Nliq, and E3SM shows small increases of Nice. These results indicate that models underestimate aerosol indirect effects on ice and mixed phase clouds over the Southern Ocean.

1 **Ice and Supercooled Liquid Water Distributions over the Southern Ocean based on In Situ**
2 **Observations and Climate Model Simulations**

3

4 Ching An Yang¹, Minghui Diao^{1,*}, Andrew Gettelman², Kai Zhang³, Jian Sun³

5 ¹Department of Meteorology and Climate Science, San Jose State University, One Washington
6 Square, San Jose, California, USA, 95192-0104

7 ²National Center for Atmospheric Research, 3450 Mitchell Ln, Boulder, CO, USA, 80301

8 ³Pacific Northwest National Laboratory, 902 Battelle Blvd, Richland, WA, USA, 99354

9

10 *Corresponding author:

11 Minghui Diao, Ph.D., Associate Professor

12 Email: Minghui.diao@sjsu.edu

13

14 **Key Points**

- 15 • Model biases of cloud occurrences and cloud phases are correlated with RH biases.
- 16 • Positive correlations are observed between aerosol concentrations and LWC, IWC, N_{liq} ,
- 17 N_{ice} , glaciation ratio, and cloud fraction.
- 18 • CAM6 and E3SM show higher (lower) LWC (IWC) by a factor of 3–100 (3–10) and
- 19 weaker aerosol indirect effects than 100-km scale observations.

20 **Abstract**

21 An evaluation of three climate models is conducted using in situ airborne observations from the
22 Southern Ocean Clouds, Radiation, Aerosol Transport Experimental Study (SOCRATES)
23 campaign. The evaluation targets cloud phases, microphysical properties, thermodynamic
24 conditions, and aerosol indirect effects at $-40^{\circ}\text{C} - 0^{\circ}\text{C}$. For cloud phase frequency distribution, the
25 Community Atmosphere Model version 6 (CAM6) shows the most similar result to the
26 observations, which allows more liquid-containing clouds below -10°C compared with its
27 predecessor – CAM5. The Energy Exascale Earth System Model (E3SM) underestimates
28 (overestimates) ice phase frequencies below (above) -20°C . Compared with 580-second averaged
29 observations (i.e., 100 km horizontal scale), CAM6 and E3SM overestimate (underestimate) liquid
30 (ice) water content (i.e., LWC and IWC), leading to lower a glaciation ratio when ice and liquid
31 coexist. Thermodynamic conditions, specifically relative humidity (RH), is likely a key factor
32 contributing to model cloud occurrence and cloud phase biases. Simulated in-cloud RH shows
33 higher minimum values than observations, possibly restricting ice growth during sedimentation.
34 As number concentrations of larger and smaller aerosols ($> 500\text{ nm}$ and $> 100\text{ nm}$) increase,
35 observations show increases in glaciation ratio, cloud fraction, LWC and liquid number
36 concentration (N_{liq}) at -18°C to 0°C , and IWC and ice number concentration (N_{ice}) at -35°C to 0°C .
37 CAM6 and E3SM show slight increases of LWC and N_{liq} , and E3SM shows small increases of
38 N_{ice} . These results indicate that models underestimate aerosol indirect effects on ice and mixed
39 phase clouds over the Southern Ocean.

40 **Plain Language Summary**

41 Clouds can be collections of entirely liquid droplets, ice particles, or both. Thermodynamic phase
42 of clouds, particularly in the Southern Ocean, contributes to large uncertainties in climate model
43 simulations. This study uses aircraft observation data to evaluate the performance of three climate
44 models. The evaluation compares model simulations with the observation data in terms of
45 environmental conditions (temperature and relative humidity), microphysical properties (amount
46 of liquid and ice), and the relationship between aerosols and clouds at temperatures from -40°C to
47 0°C. CAM5 does not allow supercooled liquid water below -10°C, while a newer version – CAM6,
48 improves the result by showing distributions of three cloud phases comparable to observations.
49 E3SM, on the other hand, has too many (few) number of liquid (ice) clouds at -35°C to -20°C. All
50 three models show an insufficient amount of ice than the observations. Model biases of cloud
51 occurrences and cloud phase are found to correlate with biases in relative humidity. The
52 observations show strong relationships between aerosols and cloud properties. As aerosol number
53 concentration increases, observations show higher cloud fraction, more ice crystals and
54 supercooled liquid droplets. The models show weaker aerosol indirect effects compared with
55 observations.

56 **Keywords:**

57 Ice and mixed phase clouds; Southern Ocean; In situ observations; Cloud phase; CAM model;
58 E3SM model.

59 1. Introduction

60 Clouds reflect shortwave radiation and re-emit terrestrial longwave radiation. They play a
61 crucial role in influencing Earth's radiation budget (Liou, 1992). The cloud types, height, the
62 partition of cloud phases, and microphysical properties of liquid droplets and ice crystals are found
63 to be important in determining the cloud radiative effect (Chen et al., 2000; Matus & L'Ecuyer,
64 2017).

65 Mixed phase clouds, clouds with the coexistence of liquid and ice, have been a focus of
66 cloud microphysics research as many of their properties remain not fully understood (e.g., Korolev
67 et al., 2017; Lohmann et al., 2016). A frequently occurring process in mixed phase clouds, named
68 the Wegener-Bergeron-Findeisen (WBF) process, describes ice crystal growth at the expense of
69 liquid droplets as the liquid droplets evaporate to water vapor that deposits on ice crystals
70 (Wegener, 1912; Bergeron, 1928). This occurs when ambient water vapor partial pressure (e) is
71 lower than the saturation vapor pressure with respect to liquid ($e_{s,liq}$) but higher than the saturation
72 vapor pressure with respect to ice ($e_{s,ice}$). The amount of ice and liquid and their mass partition in
73 mixed phase clouds are crucial for determining cloud lifetime, radiative properties, and
74 precipitation (Mülmenstädt et al., 2015; Morrison et al., 2010), as well as for developing model
75 parameterizations that represent these properties (e.g., Tan & Storelvmo, 2016; M. Zhang et al.,
76 2019).

77 Supercooled liquid water, i.e., liquid droplets that exist below 0°C in both liquid and mixed
78 phase clouds, was previously found to be underestimated in several global climate model (GCM)
79 simulations, particularly in the Southern Ocean (Bodas-Salcedo et al., 2016; Williams et al., 2013;
80 Tan et al., 2016; McCoy et al., 2016). Due to the scarcity of in situ observations in remote regions

81 such as the Southern Ocean, many evaluations of model biases rely on satellite observations (e.g.,
82 Trenberth & Fasullo, 2010; Kay et al., 2012). Guo et al. (2020), as an example, used satellite
83 retrieval data from Cloud-Aerosol Lidar and Infrared Pathfinder Satellite Observation (CALIPSO)
84 to compare with the Community Atmosphere Model version 5 (CAM5). They concluded that the
85 model misclassifies liquid as ice, leading to an underestimation of liquid cloud occurrence
86 frequencies and an overestimation of ice cloud occurrence frequencies in all vertical levels. The
87 model also shows that the supercooled liquid fraction reaches 50% at -5°C , which is much warmer
88 than the observed value of -20°C . When comparing with airborne observations around Punta
89 Arenas, Chile, D'Alessandro et al. (2019) showed that the CAM5 does not allow liquid and mixed
90 phase clouds to exist below -15°C . The model was found to overestimate and underestimate liquid
91 water content (LWC) in liquid and mixed phases, respectively, and underestimate ice water content
92 (IWC) in ice and mixed phases, which demonstrates the importance of separating three cloud
93 phases for model evaluation. Another study compared ground-based observations of mixed phase
94 clouds over the Arctic with the CAM5, and showed that revising the mixing volumes where
95 supercooled liquid water and ice particles coexist in the model can reduce the effectiveness of
96 WBF process, which prolongs the lifetime of supercooled liquid water (M. Zhang et al., 2019).
97 Klein et al. (2009) found an underestimation of the median liquid water path by a factor of three
98 in single-column models and cloud-resolving models when comparing with the observations from
99 Mixed-Phase Arctic Cloud Experiment (M-PACE). That study emphasized the importance of ice
100 microphysical processes, such as ice initiation and water vapor deposition rate on ice crystals,
101 which contribute to the underestimation of the liquid water path.

102 Thermodynamic (i.e., temperature and relative humidity), dynamic (i.e., wind speed and
103 direction), and aerosol concentration and composition are crucial for the existence of supercooled

104 liquid water (D'Alessandro et al., 2019; Fan et al., 2011; Korolev & Isaac, 2006; Gierens et al.,
105 2020; D. Zhang et al., 2019). Previously, studies showed ice, liquid and mixed phase clouds have
106 distinct relative humidity distributions. That is, relative humidity with respect to liquid (RH_{liq}) in
107 liquid clouds is close to liquid saturation, while relative humidity with respect to ice (RH_{ice}) in ice
108 clouds can deviate more from ice saturation (Fan et al., 2011; Korolev & Isaac, 2006;
109 D'Alessandro et al., 2019). For mixed phase clouds, D'Alessandro et al. (2019) showed increasing
110 deviations of RH_{liq} from liquid saturation as ice mass fraction increases in the mixture of ice and
111 liquid. Other studies also found that mixed phase clouds are influenced by vertical velocity (e.g.,
112 Korolev & Field, 2008; Shupe et al., 2008; Bühl et al., 2019) and horizontal wind direction (e.g.,
113 Gierens et al., 2020; Qiu et al., 2018) from the microscale to mesoscale. For example, Shupe et al.
114 (2008) showed that an in-cloud updraft of 0.4 m s^{-1} can sustain mixed-phase stratiform clouds in
115 the Arctic, and both cloud liquid and ice mass grow inside updrafts. Korolev and Field (2008)
116 showed that the generation of mixed-phase clouds in an ice cloud parcel requires two necessary
117 conditions for vertical velocity in theory – activating liquid water as well as increasing e to $e_{s,liq}$.
118 Bühl et al. (2019) showed that higher fluctuations in vertical velocity can lead to increasing ice
119 mass flux via primary ice production. Gierens et al. (2020) and Qiu et al. (2018) found that mixed
120 phase clouds occur more frequently in certain wind direction at Ny Ålesund, Arctic and Utqiagvik,
121 Alaska.

122 Aerosol number concentration and size distribution are also known to influence the
123 formation and evolution of ice particles and supercooled liquid water. Three hypothesized aerosol
124 indirect effects for mixed phase clouds are: (i) the glaciation indirect effect, which describes
125 increases of ice nucleating particles (INPs) that lead to more ice particles and ice phase
126 precipitation (Lohmann, 2002); (ii) the riming indirect effect, which describes increases of cloud

127 condensation nuclei (CCN) concentrations that lead to smaller liquid droplets, less riming and
128 smaller IWC (Borys et al., 2003); and (iii) the thermodynamic indirect effect, which describes
129 increases of CCN concentrations that lead to more liquid droplets, less secondary ice production
130 (Hallett & Mossop, 1974) and fewer ice particles (Rangno & Hobbs, 2001). Using airborne
131 observation data, Jackson et al. (2012) found a positive correlation between liquid number
132 concentration inside clouds and aerosol number concentration below clouds. They also found a
133 positive correlation between ice number concentration and aerosol number concentration above
134 clouds. Storelvmo et al. (2011) conducted a modeling study for aerosol indirect effects on mixed
135 phase clouds and found decreasing cloud lifetime due to increasing INP concentrations. They also
136 found decreasing ice particle sizes and increasing cloud albedo due to increasing INP
137 concentrations, which is similar to the Twomey effect on liquid clouds. These studies demonstrated
138 the importance of thermodynamic conditions and aerosol indirect effects on cloud microphysical
139 properties in the mixed phase cloud regime.

140 This study examines ice particle and supercooled liquid water distributions over the
141 Southern Ocean based on the Southern Ocean Clouds, Radiation, Aerosol Transport Experimental
142 Study (SOCRATES), and compares in situ observations with simulations of three GCMs: the
143 National Center for Atmospheric Research (NCAR) Community Atmosphere Model version 5
144 (CAM5) and version 6 (CAM6), and the Energy Exascale Earth System Model (E3SM) by the U.S.
145 Department of Energy (DOE). CAM5 and CAM6 are the atmospheric component of the NCAR
146 Community Earth System Model version 1 (CESM1) and version 2 (CESM2), respectively.
147 Compared with CAM5, CAM6 has improvements applied to mixed phase cloud parameterization,
148 prognostic precipitation species, and the interaction with aerosol schemes. E3SM uses a similar
149 physics package as CAM6 but includes many differences, such as a different dynamical core, more

150 vertical levels, a more detailed treatment of aerosol variety and properties, etc. The main goals of
151 this work are to advance the understanding of statistical distributions of cloud phase and
152 microphysical properties, the thermodynamic effect, and aerosol indirect effects on cloud
153 characteristics over the Southern Ocean, as well as to provide evaluations on three model
154 simulations.

155 In Section 2, the observation dataset and the set-up of model simulations are introduced.
156 In Section 3, case studies of three cloud segments are presented, and their thermodynamic
157 conditions (e.g., temperature and RH), cloud phases, and cloud microphysical properties are
158 compared between the observations and model simulations. Statistical distributions of cloud phase
159 occurrence frequencies, mass and number concentrations of cloud hydrometeors, effects of
160 thermodynamic conditions, and aerosol indirect effects are also analyzed based on a synthesized
161 observation dataset. Lastly, conclusions and implications are given in Section 4.

162 **2. Instrumentations and Simulations**

163 2.1 In situ airborne observations

164 The SOCRATES campaign is a flight campaign funded by the U.S. National Science
165 Foundation (NSF) and supported by NCAR. The campaign was conducted over the Australasian
166 section of the Southern Ocean region located at $62^{\circ}\text{S} - 42^{\circ}\text{S}$ and $133^{\circ}\text{E} - 164^{\circ}\text{E}$, from January 15
167 to February 24, 2018. The SOCRATES campaign aims to study clouds, aerosols, cloud-aerosol
168 interaction, precipitation, and radiation over the remote region of the Southern Ocean, where
169 climate models tend to underestimate the shortwave radiation reflected by the low-level clouds in
170 the Austral summer, especially in the colder sector of low-pressure systems. The research flights
171 often targeted cyclonic and frontal systems where the presence of strong westerly and

172 southwesterly flows along with the cold ocean surface temperatures favor the formation of low-
173 level and mid-level clouds such as stratocumulus. For this analysis, temperatures are restricted to
174 $-40^{\circ}\text{C} - 0^{\circ}\text{C}$ (also referred to as the mixed phase cloud regime hereafter), which allows for the
175 presence of both supercooled liquid water and ice particles. The SOCRATES campaign provides
176 a total of 15 research flights and 111 total flight hours at all temperatures. Among these
177 observations, 14 and 73 flight hours were at in-cloud and clear-sky conditions at $-40^{\circ}\text{C} - 0^{\circ}\text{C}$, with
178 average true airspeed at 156 and 178 m s^{-1} , respectively.

179 The NSF Gulfstream-V (GV) research aircraft is the platform used in the SOCRATES
180 campaign, with scientific instruments equipped to collect a series of data, including meteorological
181 conditions, cloud hydrometeors, total aerosol number concentrations, etc. A Rosemount
182 temperature probe measures temperature data, with an accuracy and precision of $\pm 0.3\text{ K}$ and 0.01
183 K , respectively. The Fast-Two Dimensional Cloud probe (Fast-2DC) and cloud droplet probe
184 (CDP) were mounted underneath the aircraft wings to measure cloud properties including LWC,
185 IWC, and liquid and ice number concentrations (N_{liq} and N_{ice}) at 1-Hz resolution. The CDP
186 measures particle sizes from 2 to $50\text{ }\mu\text{m}$, while Fast-2DC measures larger particle sizes from 62.5
187 to $1600\text{ }\mu\text{m}$. In addition, the Fast-2DC probe mathematically reconstructs particles up to $3200\text{ }\mu\text{m}$.
188 The Fast-2DC probe also captures particle images with a resolution of $25\text{ }\mu\text{m}$ by recording the
189 shadows of hydrometeors as they pass through a laser beam. Mounted next to the Fast-2DC, the
190 Ultra-High Sensitivity Aerosol Spectrometer (UHSAS) measures the number concentrations and
191 size distributions of aerosols in the 60 to 1000 nanometer (nm) range. Another instrument, the
192 Vertical Cavity Surface Emitting Laser (VCSEL) hygrometer, was mounted on top of the aircraft
193 and reported water vapor molecule number density at 25-Hz resolution with an accuracy of $\sim 6\%$
194 and a precision of $\leq 1\%$ (Zondlo et al., 2010). Its product of water vapor mixing ratio was reported

195 in 1-Hz resolution, and a PI-calibrated dataset of water vapor mixing ratio is used in this study
196 based on post-campaign laboratory calibration in summer 2018 (Diao, 2020). Water vapor and
197 temperature data are used to calculate RH_{liq} and RH_{ice} by using the equations for $e_{s,liq}$ and $e_{s,ice}$ in
198 Murphy and Koop (2005), respectively. Combining the uncertainties from water vapor and
199 temperature measurements, the uncertainties for RH_{ice} are 6.9% – 6.5%, and the uncertainties for
200 RH_{liq} are 6.8% – 6.4% from -40°C to 0°C , respectively.

201 The observed cloud phases are determined based on the cloud phase identification method
202 from Figure 1 of D’Alessandro et al. (2019). Measurements from CDP are categorized into three
203 types (i.e., large aerosols, liquid droplets, and ice particles) based on various thresholds of particle
204 number concentration (N_{CCDP}) and mass concentration (M_{CCDP}). That is, particles with $N_{CCDP} \leq$
205 $10^{-1.5} \text{ cm}^{-3}$ and $M_{CCDP} \leq 10^{-3.4} \text{ g m}^{-3}$ are considered large aerosols; particles with $10^{-1.5} < N_{CCDP} <$
206 $10^{-0.5} \text{ cm}^{-3}$ and $M_{CCDP} > 10^{-3.4} \text{ g m}^{-3}$ are defined as ice particles; and particles with $N_{CCDP} \geq 10^{-0.5}$
207 cm^{-3} and $M_{CCDP} > 10^{-3.4} \text{ g m}^{-3}$ are defined as liquid droplets. For the Fast-2DC probe, if the ambient
208 temperature $\geq -30^{\circ}\text{C}$, particle number concentration (N_{C2DC}), the maximum particle diameter
209 (D_{max_2DC}), and the standard deviation of size distribution (σ_{D_2DC}) are used to categorize liquid
210 droplets and ice particles. If the ambient temperature $< -30^{\circ}\text{C}$, a check of CDP reading is also
211 required. The total LWC and IWC are based on the combined measurements of both probes. Cloud
212 phases are defined by using the mass fraction of ice (hereafter named as the glaciation ratio), i.e.,
213 IWC/CWC , where CWC stands for cloud water content and equals the sum of LWC and IWC
214 (Korolev and Isaac, 2003; D’Alessandro et al. 2019). Ice, mixed and liquid phases are defined
215 when glaciation ratio > 0.9 , $0.1 \leq \text{glaciation ratio} \leq 0.9$, and glaciation ratio < 0.1 , respectively.

216 2.2 Three GCM simulations

217 This study evaluates three model simulations against the in situ observations, including the
218 NCAR CESM1 / CAM5 model, an updated version CESM2 / CAM6 model, and the DOE E3SM
219 / Atmosphere Model version 1 (EAMv1). Figure 1 shows the map of aircraft flight tracks and the
220 collocated model output from three simulations.

221 Both CAM5 and CAM6 use a finite-volume dynamical core (Lin et al., 2004). The two
222 models were run with a resolution of $0.9^\circ \times 1.25^\circ$ and 32 vertical levels, a time step of 30 minutes,
223 and were nudged towards MERRA-2 temperature and horizontal wind field reanalysis data. The
224 model output was saved at the closest location to the aircraft flight track for every 10-minute
225 observations, which facilitates a more direct comparison between the simulations and observations.
226 Both CAM5 and CAM6 were run with a spin-up time of one year, and a relaxation time of 24
227 hours when nudged towards the reanalysis data. The CAM5 simulation uses the MG1 cloud
228 microphysics scheme (Morrison & Gettelman, 2008) coupled with a modal aerosol module with
229 three modes (MAM3) (Liu et al., 2012). A detailed description of CAM5 was previously
230 documented in Neale et al. (2012). The newer version, CAM6, uses cloud microphysics scheme
231 MG2 with additional improvements of ice nucleation, ice microphysics, prognostic precipitation
232 species, and interaction with aerosol schemes to calculate cloud mass fractions and number
233 concentrations (Gettelman & Morrison, 2015). The MG2 microphysics scheme is coupled with an
234 updated modal aerosol module with four modes, MAM4 (Liu et al., 2016). The MAM4 has an
235 additional aerosol mode named primary carbon compared with MAM3, and has improvements to
236 aerosol resuspension, nucleation, scavenging, and sea spray emissions. CAM6 also uses Cloud
237 Layers Unified By Binormals (CLUBB) for turbulence and shallow convection, which replaces
238 the original shallow convection scheme in CAM5 (Park & Bretherton, 2009).

239 The DOE E3SM / EAM version 1, on the other hand, is a derivative of CAM6 with a
240 spectral element dynamical core and modified physics parameterization schemes (Rasch et al.,
241 2019). The vertical and horizontal resolutions of E3SM are 72 layers and ne30 (1°), respectively.
242 A nudged simulation towards ERA5 temperature and horizontal wind was performed, with a
243 relaxation time scale of 6 hours (Sun et al., 2019). The output closest to flight track location at a
244 10-minute frequency is used for the comparison. The E3SM nudged simulation started on
245 December 1, 2017 and was initialized with the initial condition output for December from a
246 climatological run (for both atmosphere and land). This allows a relatively short simulation time
247 for the model to spin up compared with using the default initial condition file. Similar to CAM6,
248 E3SM also uses the MG2 microphysics scheme and MAM4, but with more detailed treatments of
249 aerosol categories and processes such as light-absorbing particle deposition.

250 2.3 Approaches to facilitate comparisons between model simulations and observations

251 Due to differences of spatiotemporal resolutions and various definitions of cloud and
252 aerosol variables between in situ observations and model simulations, several approaches are used
253 to select collocated samples and recalculate model output variables for comparisons. First, for
254 model output in an entire atmospheric column, only the model grid box with the closest location
255 to the vertical location of the aircraft is selected. Second, since simulated cloud hydrometeors in
256 the model cover the size range from zero to infinity, which exceeds the sampling range of CDP
257 and Fast-2DC probes, a size cutoff is applied to all simulated cloud properties by restricting the
258 particle size to a discrete range of 2 to 50 μm plus 62.5 to 3200 μm . This method was previously
259 used in several model-observation comparison studies, such as Eidhammer et al. (2014) and Patnaude
260 et al. (2020). The model output variables being processed for this partial size range include “LWC”,
261 “NUMLIQ”, “IWC”, “NUMICE”, “AQSNOW” and “ANSNOW”. These variables represent grid-

262 average values for mass and number concentrations of liquid, ice, and snow, respectively. The
263 simulated LWC and N_{liq} are defined by the size-restricted “LWC” and “NUMLIQ”, respectively.
264 We further define the simulated IWC as the sum of size-restricted “IWC” and “AQSNO” and
265 the simulated N_{ice} as the sum of size-restricted “NUMICE” and “ANSNO”, which means that
266 the simulated ice phase includes both ice crystals and snow since cloud measurements in the
267 observations include both ice crystals and snow. Aerosol number concentrations (N_a) from the
268 simulations are also restricted to aerosol sizes ≤ 1000 nm based on a log-normal distribution, which
269 follows the size range of the UHSAS measurements. The RH_{ice} and RH_{liq} values in the simulations
270 are calculated based on water vapor specific humidity and the saturation vapor pressure equations
271 from Murphy and Koop (2005), which avoids using the RH variable directly reported by the model.
272 The simulated RH_{liq} shows the maximum values at 101%, 100%, and 105% for CAM6, CAM5,
273 and E3SM, respectively. For the observations, RH_{liq} values greater than 105% are set as NAN
274 values (processed for 2535 seconds) due to the combined uncertainties from water vapor and
275 temperature measurements. For in-cloud conditions, the observations define them as where at least
276 one cloud hydrometeor has been detected by either CDP or Fast-2DC probe. The maximum and
277 minimum values of LWC (IWC) in the observations are 1.41 and 5.01×10^{-5} g m⁻³ (55.79 and
278 5.68×10^{-5} g m⁻³), respectively. For simulations, if IWC or LWC is less than 10^{-7} g m⁻³, they are not
279 considered as real hydrometeors and are set to zero. This means that for simulations, in-cloud
280 conditions are defined as either IWC or LWC being greater than 10^{-7} g m⁻³, while the remaining
281 conditions are considered as clear sky. In addition, only N_{liq} and N_{ice} greater than 10^{-7} cm⁻³ are
282 used in the analysis of simulations. Table 1 summarizes the maximum and minimum values for
283 thermodynamic conditions (i.e., temperature, pressure, RH_{ice} , and RH_{liq}) and cloud microphysical
284 properties (i.e., LWC, IWC, N_{liq} , and N_{ice}) used for the analysis of observations and simulations.

285 To examine the effect of spatial scales to the comparison results, 1-Hz observations are
286 averaged by various scales, including 200 seconds (i.e., 34.5 km horizontal resolution, since the
287 average true airspeed of the aircraft at -40°C to 0°C is 172 m s^{-1}) and 580 seconds (i.e., 100 km
288 horizontal resolution) using a moving average method similar to D'Alessandro et al. (2019). This
289 moving average generally leads to smaller values of average IWC, LWC, N_{ice} , and N_{liq} in coarser
290 scale data compared with the 1-s data, since the coarser scale data include both clear-sky and in-
291 cloud segments during the averaging process. Since these observation data represent averages over
292 the entire length scale, they are comparable with simulated grid-average cloud quantities.

293 **3. Results**

294 *3.1 Three case studies of cloud phases, microphysical properties and thermodynamic conditions*

295 Individual flight segments from the SOCRATES campaign are selected to illustrate three
296 typical situations: (i) an ice-dominated condition, (ii) a liquid-dominated condition, and (iii) a
297 heterogeneous mixture of ice, liquid, and mixed phases.

298 A segment from research flight (RF) 04 represents a homogeneous segment of ice phase
299 (Figures 2 and 3). The thermodynamic condition for this segment is ideal for ice formation with a
300 temperature constantly around -32°C and the magnitude of ice supersaturation (i.e., $\text{RH}_{\text{ice}} - 1$)
301 around 10% – 50% (Figure 2 a). The IWC values, derived from the 1-Hz CDP and 2DC
302 measurements, are above 0.01 g m^{-3} for most of the in-cloud conditions (Figure 2 b). The 2DC
303 imageries of cloud hydrometeors confirm ice phase samples defined by the cloud phase
304 identification method (Figure 2 d and e).

305 The model simulations either miss part of the in-cloud segment or misidentify the cloud
306 phase (Figure 2 c). These biases are well correlated with biases seen in the RH conditions (Figure
307 3 b and c). The CAM6 misses the first 7 minutes (UTC 00:43:00 – 00:50:00) of the in-cloud
308 segment but overestimates IWC in a later segment (UTC 01:03:20 – 01:06:40) when it should be
309 clear sky. CAM5 captures the ice phase in the beginning, possibly attributed to the simulated RH_{ice}
310 by CAM5 being closer to observations than CAM6 at this time range. Even though E3SM shows
311 smaller temperature biases than CAM6 and CAM5, it misses the in-cloud segment in the first 16
312 minutes (UTC 00:43:00 – 00:59:00) and also misidentifies the observed ice phase as mixed phase.
313 These two biases shown in E3SM are correlated with a low RH_{ice} bias of 60% in the earlier segment
314 and a high RH_{ice} bias of 20% – 50% at the later segment, respectively. In fact, in the later segment,
315 E3SM shows RH_{liq} at liquid saturation, which produces false LWC at 0.03 g m^{-3} and N_{liq} at 5 cm^{-3}
316 ³ that should have been zero (Figure 3 e and g). Compared with 1-s observations, simulated IWC
317 is 2 orders of magnitude smaller in CAM5, and 3 orders of magnitude smaller in CAM6 and E3SM
318 between 00:50:30 and 01:01:00. Simulated N_{ice} in CAM5 is one order of magnitude higher than
319 observations for the middle part of the segment, while CAM6 and E3SM show similar N_{ice} to the
320 1-s observations. Glaciation ratios of CAM5 and CAM6 follow the observed value at unity for ice
321 phase, while E3SM shows very low glaciation ratios due to the false values of LWC at the later
322 segment.

323 A segment from RF06 was selected to show a liquid-dominated segment with relatively
324 homogeneous distributions of supercooled liquid water in UTC 02:31:40 – 02:43:00 (Figures 4
325 and 5). In this case, the observed temperature ranges from -2°C to -4°C and the RH_{liq} remains at
326 or slightly below liquid saturation (Figure 4 a), favoring the existence of supercooled liquid water.
327 All models have temperature and RH well matched with the observations (Figure 5 a – c), yet

328 differences in simulated IWC and LWC (Figure 5 d and e) lead to varying results of cloud phases.
329 That is, E3SM simulates mixed phase for the entire segment while CAM5 and CAM6 show both
330 mixed and liquid phases. Between UTC 02:28:20 – 02:31:40, ice particles coexist with supercooled
331 liquid water. This heterogeneous segment is identified as mixed phase by CAM5 and E3SM but
332 as liquid phase in CAM6. The IWC ($0.01 - 10 \text{ g m}^{-3}$) and N_{ice} ($0.01 - 0.1 \text{ cm}^{-3}$) in 1-s observations
333 are underestimated in the simulations by 2 and 0.5 – 2 orders of magnitude, respectively. In the
334 later segment UTC 02:31:20 – 02:43:20, all three models produce spurious ice particles, leading
335 to higher glaciation ratios than the value (zero) in 1-s observations. Both CAM6 and E3SM show
336 similar LWC and N_{liq} to observations within one order of magnitude, while CAM5 shows lower
337 LWC and N_{liq} than observations by 1.5 and 1 orders of magnitude, respectively.

338 Figures 6 and 7 show an example of heterogeneously mixed ice particles and supercooled
339 liquid water from RF03. During UTC 00:41:40 – 00:52:30, temperatures remain relatively constant
340 at -3°C , while RH_{liq} varies between 90% and 105% (Figure 6 a), which partly contributes to the
341 heterogeneous distributions of clear-sky conditions and three cloud phases. Cloud imageries of the
342 Fast-2DC probe verify the identification of three cloud phases (Figure 6 d – f). Both CAM models
343 show the same results as they mainly identify mixed phase only. In contrast, E3SM mainly
344 identifies ice phase only. All simulated temperatures are within 1°C around the observed values.
345 Simulated RH_{liq} are almost identical in CAM6 and CAM5 at liquid saturation, while E3SM shows
346 RH_{liq} at 95% – 97%, which leads to a less favorable condition of supercooled liquid water and
347 likely causes the missing LWC in E3SM. Consistent with results from RF04 and RF03, all three
348 models underestimate IWC by 1 – 2 orders of magnitude compared with 1-s observations, while
349 LWC simulated by CAM6 is the most similar to the observed values. During UTC 00:47:30 –
350 00:52:40, the 1-Hz observations show glaciation ratio mostly at one, but CAM5 and CAM6 show

351 glaciation ratio around 0.6 and 0.2, respectively, due to the underestimation of IWC. Even though
352 E3SM shows a glaciation ratio at one for this segment, it is due to the combined effects of
353 underestimating IWC and missing LWC.

354 *3.2 Cloud phase occurrence frequency and distributions of LWC, IWC and glaciation ratio*

355 Cloud phase occurrence frequencies for the entire SOCRATES campaign are compared
356 with model simulations (Figure 8). The number of samples for three cloud phases is shown in the
357 supplementary Figure S1. Figure 8 b and c show the cloud phase occurrence frequencies for 200 s
358 and 580 s spatially averaged observation (horizontal scales of 35 and 100 km, respectively). An
359 increase in spatial scale also increases the occurrence frequencies of mixed phase between -35°C
360 to 0°C by a factor of 2 – 4, i.e., mixed phase frequencies are 0.05 – 0.1 for 1-s observations,
361 compared with 0.1 – 0.3 for 200-s and 0.1 – 0.4 for 580-s observations. The increase of mixed
362 phase frequency is compensated by the reduction of liquid and ice phase frequency above and
363 below -20°C , respectively.

364 Simulations are further examined with two types of simulated IWC – one contains both ice
365 crystals and snow (Figure 8 d – f) which is used as the default definition of simulated LWC, while
366 the other contains only ice crystals (g – i). Excluding snow as part of the simulated IWC increases
367 (decreases) liquid (mixed) phase frequency by 0.1 – 0.2 in three simulations. Compared with the
368 580-s observations, CAM6 (Figure 8 d) shows the most similar cloud phase frequencies for ice,
369 liquid, and mixed phases. The minor issue with CAM6 is slightly lower (higher) mixed (liquid)
370 phase frequency by 0.1 at -20°C to 0°C than 580-s averaged observations. CAM6 significantly
371 improves the presence of supercooled liquid water below -10°C compared with CAM5, which
372 shows zero frequency of liquid-containing clouds below -10°C . The lack of supercooled liquid

373 water below -10°C in CAM5 was also shown in the previous work of D'Alessandro et al. (2019).
374 E3SM (Figure 8 f) underestimates (overestimates) the frequency of ice phase clouds below (above)
375 -20°C by 0.1 compared with 580-s averaged observations. E3SM was found to overestimate of
376 liquid cloud fraction between -20°C and -30°C at high latitudes (Y. Zhang et al., 2019). It was also
377 found to underestimate pure ice clouds at most temperatures except for close to -40°C based on a
378 global-scale evaluation (Rasch et al., 2019). A similar result of E3SM overestimating supercooled
379 liquid water below -20°C was also documented in Zhang et al. (2020) for an analysis of Arctic
380 clouds.

381 Effects of spatial scales are examined in Figure 9 a – c for observations that are spatially
382 averaged by every 10 s, 50 s, 100 s, 200 s, 290 s, and 580 s, which represent horizontal scales of
383 1.7, 8.6, 17, 35, 50 and 100 km, respectively. The overall trend of an increasing liquid (ice) phase
384 frequency in a warmer (colder) environment remains unchanged. Larger spatial scales consistently
385 show increase in the occurrence frequencies of mixed phase between -35°C to 0°C . Furthermore,
386 length scales of three cloud phases in 1-Hz observations are examined in Figure 9 d – f. The
387 number of samples for Figure 9 is shown in supplementary Figure S2. Length scales of individual
388 cloud phase segments are calculated by the consecutive seconds of the same cloud phase in 1-Hz
389 observations. The shorter and longer length scales represent more heterogeneous and
390 homogeneous distributions of cloud phases, respectively. The observations show more mixed
391 phase segments at shorter length scales (1–3 seconds) than longer length scales (> 10 seconds),
392 while the liquid and ice phases dominate the longer length scales (> 10 seconds). This result
393 indicates that the coexistence of ice and liquid occurs more frequently at shorter length scales,
394 likely due to the effective transition from liquid to ice via the WBF process.

395 Cloud microphysical properties, i.e., LWC, IWC, and glaciation ratios are examined for
396 various temperatures (binned by 5°C) in Figure 10. The number of samples for this analysis is
397 shown in supplementary Figure S3. 1-s, 200-s, and 580-s averaged observations are compared with
398 model simulations. Averaging observations over 200 seconds significantly reduces the average
399 LWC and IWC by 1 – 2 orders of magnitude compared with 1-s data, while the 580-s averaged
400 observations show further reduction of LWC and IWC by up to 0.5 order of magnitude. Compared
401 with 580-s averaged observations, CAM6 (E3SM) shows similar average LWC to the observations
402 above -5°C (-15°C) but lower average LWC at lower temperatures by 0.5 – 2 orders of magnitude.
403 Consistent with Figure 8, CAM5 lacks LWC below -10°C. For the average IWC, all three models
404 underestimate IWC by 1 – 2, 0.5 – 1.5, and 0.5 – 1 orders of magnitude compared with 1-s, 200-s,
405 and 580-s observations, respectively.

406 Two types of glaciation ratios are calculated, one is for all in-cloud conditions (Figure 10
407 g – i), and the other one for conditions with coexisting ice particles and supercooled liquid water
408 only (j – l). For the former type, the glaciation ratios are controlled by the ratios between ice phase
409 and liquid phase occurrence frequencies, the two dominant phases. For the latter type, the
410 glaciation ratios are controlled by the mass partitioning between ice and liquid when they coexist.
411 For the former type of glaciation ratios, observations and CAM6 show similar results (Figure 10
412 g), consistent with their similar cloud phase frequencies in Figure 8. The latter glaciation ratios in
413 CAM6 (Figure 10 j) are significantly lower than the 580-s averaged observations by 0.3 – 0.8, due
414 to the underestimation of IWC in the model. E3SM overestimates the former type of glaciation
415 ratios above -20°C, and underestimates the latter type of glaciation ratios below -20°C. These
416 analyses show that even though CAM6 produces glaciation ratios of all in-cloud conditions very

417 similar to the observations, its underestimation of IWC leads to large biases of mass partitioning
418 inside the mixture of ice and liquid.

419 A similar analysis to Figure 10 is done using simulated IWC containing only ice crystals
420 (supplementary Figure S4). When excluding snow in the simulated IWC, even larger model biases
421 of IWC by a factor of 2 – 3 are seen compared with including snow in the simulated IWC.
422 Additionally, a sensitivity test is conducted to examine the impacts of model output frequency, by
423 using E3SM output that is closest to every 1 second, 1 minute, and 10 minutes of observations
424 (supplementary Figure S5). The results show very similar results for cloud phase frequencies,
425 average LWC, IWC and glaciation ratios under various model output frequencies.

426 *3.3 Thermodynamic conditions for clear-sky, in-cloud conditions and three cloud phases*

427 Thermodynamic conditions are crucial for the formation of ice particles and supercooled
428 liquid water, as illustrated in the case studies in Section 3.1. Figure 11 shows probability density
429 functions (PDFs) of temperature and RH_{ice} categorized by in-cloud and clear-sky conditions (top
430 two rows) and three cloud phases (bottom two rows). The PDF is calculated as the number of
431 samples of a certain condition (such as in-cloud) at each bin divided by the total number of samples
432 of that condition in all bins. PDFs of temperatures are comparable between observations and
433 simulations. PDFs of RH_{ice} for in-cloud conditions in the simulations show lower maximum values
434 (CAM6 134%, CAM5 116%, E3SM 144%) compared with 1-s observations (147%), but the
435 simulated values of CAM6 and CAM5 are closer to 580-s averaged observations (127%). Similarly,
436 PDFs of RH_{ice} for clear-sky conditions in the simulations show lower maximum values (CAM6
437 111%, CAM5 104%, E3SM 125%) than 1-s observations (142%) but are closer to 580-s averaged
438 observations (109%). The simulations also underestimate the frequencies of sub-saturated

439 conditions for in-cloud RH_{ice} , since the 1-s and 580-s averaged observations show minimum in-
440 cloud RH_{ice} at 4% and 8%, respectively, while simulations show minimum values of 25% – 66%.

441 In terms of PDFs of RH_{ice} in three cloud phases, the peak positions of RH_{ice} in 1-s
442 observations are located around 100% – 102% for all three phases. For 580-s observations, the
443 peak positions are located at lower values (~90%) due to the inclusion of clear-sky segments in
444 the averaging process. Three simulations show peaks of in-cloud RH_{ice} around 100%, but with
445 narrower ranges for all three cloud phases. For both observations and simulations, mixed phase is
446 associated with a narrower RH_{ice} range than ice and liquid phases, consistent with the theoretical
447 condition for WBF process with $e_{s,ice} < e < e_{s,liq}$. The lack of sub-saturated conditions for ice phase
448 may contribute to the underestimation of ice growth and the riming effect during sedimentation,
449 which possibly leads to lower IWC in the simulations.

450 *3.4. Aerosol indirect effects on cloud microphysical properties*

451 In this section, aerosol indirect effects on cloud microphysical properties at various
452 temperatures are examined based on the relationships between total aerosol number concentrations
453 (Na) and cloud microphysical properties (Figures 12 – 14). Since CAM5 significantly
454 underestimates the amount of supercooled liquid water below -10°C, the model evaluation in this
455 section focuses on CAM6 and E3SM only. The number of samples related to these figures is shown
456 in supplementary Figures S6 and S7. The analysis is based on Na separated into two groups –
457 aerosols with diameters > 500 nm (hereafter named as Na_{500}) and > 100 nm (named as Na_{100}).
458 Previously, DeMott et al. (2010) showed that at temperatures higher than -36°C, Na_{500} is well
459 correlated with number concentrations of INPs, which can facilitate ice crystal formation during
460 heterogeneous nucleation.

461 For the impacts of larger aerosols, as $\log_{10}(N_{a500})$ increases, the 1-Hz observations show
462 increasing LWC and N_{liq} between -18°C and 0°C , and increasing IWC and N_{ice} between -35°C and
463 0°C (Figure 12), indicating Twomey effects on both liquid droplets and ice particles at these
464 temperature ranges. Similar effects are also present in the 580-s observations, indicating that these
465 aerosol indirect effects are consistently observed from horizontal scales of hundreds of meters to
466 100 kilometers. Between -25°C and -18°C , higher N_{a500} values were observed ($> 1000 \text{ cm}^{-3}$). A
467 significant increase of IWC (up to 10 g m^{-3}) and N_{ice} (up to 0.1 cm^{-3}) are seen at higher N_{a500} values
468 at this temperature range, starting from N_{a500} as low as 3 cm^{-3} . This feature indicates a possible
469 existence of effective INPs at this level, while future work is warranted to investigate the origins
470 of these larger aerosols. LWC and N_{liq} at this level are also lower than those at temperatures above
471 -18°C , possibly due to more effective evaporation of liquid droplets via the WBF process when
472 more ice particles exist.

473 The analysis of N_{a100} (Figure 13) shows similar results to N_{a500} , that is, as N_{a100} increases,
474 increasing IWC and N_{ice} are seen from -35°C to 0°C with a strong increase between -25°C
475 and -18°C . On the other hand, LWC and N_{liq} increase with increasing N_{a100} from -18°C to 0°C ,
476 and the LWC and N_{liq} at -25°C to -18°C are lower than those at -18°C to 0°C by 2 orders of
477 magnitude.

478 In terms of model simulations, both CAM6 and E3SM capture the decreasing trend of
479 maximum N_{a500} and N_{a100} as temperature decreases, yet the maximum values of simulated N_{a500}
480 and N_{a100} are 10 and 100 cm^{-3} , respectively, which are 2 orders of magnitude smaller than the
481 580-s observations. For aerosol indirect effects on liquid droplets, CAM6 and E3SM show smaller
482 increases of LWC and N_{liq} when N_{a500} and N_{a100} increase between -15°C and 0°C . That is, the
483 580-s observations show LWC and N_{liq} increase 2 – 3 orders of magnitude when N_{a500} increases

484 from 0.01 cm^{-3} to 3.2 cm^{-3} , while LWC and N_{liq} increase 1 (0.5) order of magnitude in CAM6
485 (E3SM). For aerosol indirect effects on ice particles, E3SM shows increases of N_{ice} by 1 – 2 orders
486 of magnitude when N_{500} increases from 0.01 cm^{-3} to 3.2 cm^{-3} at a narrow temperature range
487 between -20°C and -10°C , smaller than the increases seen in the observations (~ 2 orders of
488 magnitude). Almost no effects on IWC are seen in CAM6 or E3SM. Overall, these results indicate
489 that the models underestimate aerosol indirect effects on both liquid droplets and ice particles.

490 Aerosol indirect effects on phase partitioning and cloud fraction are examined in Figure 14.
491 Two types of glaciation ratios are examined – for all in-cloud condition (a–h) and coexisting ice
492 and liquid only (i–p). For the glaciation ratios of all in-cloud conditions, the observations show
493 both temperature effect and aerosol indirect effect, that is, glaciation ratios increase with
494 decreasing temperature as well as with increasing N_{500} and N_{100} . When larger aerosols exist,
495 observations show that glaciation ratios mostly reach unity below -20°C (Figure 14 a and b). The
496 significant increase of glaciation ratios with increasing N_{500} and N_{100} at -25°C – -18°C is
497 consistent with the large increase of IWC in Figures 12 and 13. At temperature above -18°C ,
498 increase of glaciation ratio is also observed at higher Na. The second type of glaciation ratios for
499 coexisting ice and liquid also shows an increasing trend with increasing N_{500} and N_{100} , although
500 fewer samples are seen at unity than the first type of glaciation ratios. This indicates that the phase
501 partitioning within the mixture of ice and liquid is less affected by Na, but the phase partitioning
502 among all three cloud phases is affected by Na more strongly.

503 For both CAM6 and E3SM, only temperature effect is seen and no aerosol indirect effects
504 are seen on either type of glaciation ratios, which is consistent with the lack of aerosol indirect
505 effects on ice particles in Figures 12 and 13. Cloud fraction is calculated by normalizing the
506 number of in-cloud samples in each bin by the total number of samples in that bin. Note that the

507 cloud fraction for simulations is not based on the model output “cloud fraction”, but rather is
508 calculated based on the in-cloud definition described in Section 2.3. 100% cloudiness is seen in 1-
509 s (580-s) observations at $N_{a500} > 3 \text{ cm}^{-3}$ ($> 0.1 \text{ cm}^{-3}$) and $N_{a100} > 300 \text{ cm}^{-3}$ ($> 100 \text{ cm}^{-3}$). Both
510 CAM6 and E3SM show a slight increase of cloud fraction from below to above -15°C , yet no clear
511 relationship between cloud fraction and aerosol concentrations is seen.

512 **4. Conclusions and Implications to Model Development**

513 This study focuses on examining cloud characteristics at -40°C to 0°C over the Southern
514 Ocean based on in situ aircraft-based observations and three GCM simulations (i.e., CAM6, CAM5,
515 and E3SM). A series of cloud characteristics are examined, including cloud phases, mass and
516 number concentrations of cloud hydrometeors, phase partitioning, thermodynamic conditions, and
517 aerosol indirect effects. Several approaches are used to facilitate the comparison between in situ
518 observations and GCM simulations, including using nudged simulations toward reanalysis data,
519 recalculating cloud properties based on instrument measurement ranges, and examining the
520 impacts of spatial scales on the comparison results.

521 Spatially averaging observation data from 1 s to 580 s (i.e., from $\sim 0.2 - 100$ km in
522 horizontal) is found to affect several variables, such as reducing average LWC and IWC by 1 – 2
523 orders of magnitude due to the inclusion of clear-sky segments in the grid-mean averages,
524 increasing the occurrence frequency of mixed phase clouds since ice particles and supercooled
525 liquid water are more likely to coexist at coarser scales, reducing the maximum RH_{ice} for in-cloud
526 and clear-sky conditions, and decreasing the peak positions of RH_{ice} PDFs for three cloud phases.
527 For other characteristics, spatial averaging has a small impact on the average glaciation ratios of

528 all in-cloud conditions, and the positive correlations of LWC, IWC, N_{liq} , and N_{ice} with respect to
529 aerosol number concentrations.

530 Evaluation of three model simulations shows that CAM6 has the most similar cloud phase
531 occurrence frequency to observations compared with CAM5 and E3SM. Particularly, CAM6 and
532 E3SM significantly improve the proportion of liquid and mixed phase clouds below -10°C
533 compared with the CAM5. This is most likely due to the removal of a temperature-dependent mass
534 partitioning function between ice and liquid in the shallow convection scheme (Park & Bretherton,
535 2009) that was previously used in CAM5, as discussed in previous studies (Gettelman et al., 2020;
536 Kay et al., 2016). E3SM underestimates (overestimates) ice phase frequencies below
537 (above) -20°C . When evaluating simulated LWC compared with 580-s observations, CAM6 and
538 E3SM overestimate LWC values by 0.5 – 2 orders of magnitude below -5°C and -15°C ,
539 respectively. Another main model bias is the underestimation of IWC at all temperatures between
540 -40°C and 0°C by 0.5 – 1 orders of magnitude compared with 580-s observations. Even though
541 CAM6 shows small biases of glaciation ratios of all in-cloud conditions (i.e., with biases less than
542 ± 0.1), it significantly underestimates glaciation ratios of coexisting ice and liquid by 0.3 – 0.8 due
543 to the underestimation of IWC.

544 Thermodynamic conditions, specifically RH, are found to be well correlated with model
545 biases of cloud occurrences and cloud phases as illustrated in case studies. This result combined
546 with the previous study (Wu et al., 2017) which showed that RH biases in the CAM5 are dominated
547 water vapor biases indicates that the representation of water vapor distribution is important for
548 simulating clouds over the Southern Ocean. In terms of PDFs of in-cloud RH_{ice} , 1-s observations
549 show larger variabilities of in-cloud RH_{ice} ranging from 4% to 147%, while the simulations show
550 narrower ranges, i.e., 25%–134% for CAM6, 52%–116% for CAM5, and 66%–144% for E3SM.

551 When averaging the observations into every 580 s, the observed in-cloud RH_{ice} is seen from 8% to
552 127%, indicating that the simulations lack of sub-saturation at in-cloud conditions . This may limit
553 the ranges of cloud microphysical properties, such as underestimating IWC by limiting ice growth
554 and riming in sub-saturated conditions.

555 Regarding aerosol indirect effects on cloud microphysical properties, positive correlations
556 are found between cloud microphysical properties (IWC, LWC, N_{ice} , and N_{liq}) and the number
557 concentration of larger and smaller aerosols (i.e., Na_{500} and Na_{100} , respectively), suggesting the
558 Twomey effect on ice particles at $-35^{\circ}C$ to $0^{\circ}C$, and on supercooled liquid water from $-18^{\circ}C$ to
559 $0^{\circ}C$. The increase of LWC and N_{liq} with increasing Na are stronger at warmer conditions ($-18^{\circ}C$
560 to $0^{\circ}C$), possibly due to less activation of ice nucleation at this temperature range and therefore
561 less reduction of LWC and N_{liq} due to the WBF process. On the other hand, aerosol indirect effects
562 on IWC and N_{ice} are stronger at $-25^{\circ}C$ – $-18^{\circ}C$, indicating possible effective INPs at this vertical
563 level. Higher glaciation ratios of all in-cloud conditions are also found to be associated with higher
564 Na and lower temperatures in both 1-s and 580-s observations. Small increases of LWC and N_{liq}
565 with increasing Na are seen in CAM6 and E3SM between $-15^{\circ}C$ to $0^{\circ}C$, yet the models miss the
566 increasing IWC and N_{ice} with increasing Na at $-25^{\circ}C$ to $-18^{\circ}C$. Small increases of N_{ice} are seen in
567 E3SM only at a narrow temperature range ($-20^{\circ}C$ to $-10^{\circ}C$), while no obvious aerosol indirect
568 effects are seen on IWC, cloud fraction or either type of glaciation ratios in CAM6 and E3SM.
569 These results suggest that stronger aerosol indirect effects on both liquid droplets and ice particles
570 should be considered for future development of cloud microphysics parameterizations, especially
571 since model parameterizations still have limited aerosol types acting as INPs. In addition, the
572 maximum Na_{500} and Na_{100} values are underestimated in CAM6 and E3SM by 1 – 2 orders of
573 magnitude compared with 580-s observations, suggesting that higher concentrations of INPs and

574 cloud condensation nuclei (CCN) need to be included in the model. In fact, higher CCN number
575 concentration has also been recommended in another model evaluation study on CAM6 by
576 Gettelman et al. (2020).

577 Overall, this study provides a series of metrics for model evaluation of ice, liquid, and
578 mixed phase clouds at -40°C to 0°C based on high resolution, in situ observations. Both
579 thermodynamic conditions and aerosol number concentrations are found to be important factors in
580 controlling cloud phases, the mass partition of ice and liquid, and cloud hydrometeor mass and
581 number concentrations. The model evaluation in this study is restricted to default configurations
582 of three GCMs, while future work is warranted to investigate the impacts of individual parameters
583 in cloud microphysics parameterizations that may lead to improved results compared with
584 observations. The observation-based statistical distributions of cloud phase frequency,
585 microphysical properties, and their correlations with temperature, RH, and aerosol concentrations
586 can be used to guide future model development at various horizontal scales.

587 **Acknowledgement**

588 C. Yang and M. Diao acknowledge funding from the NSF Division of Atmospheric and Geospace
589 Sciences (AGS) grant #1642291 and NSF Office of Polar Programs (OPP) grant #1744965. M.
590 Diao also acknowledges funding from the Department of Energy (DOE) Atmospheric System
591 Research (ASR) grant DE-SC0021211, and the support of the NCAR Advanced Study Program
592 (ASP) Faculty Fellowship in 2016 and 2018. C. Yang received the Walker Fellowship from San
593 Jose State University. A. Gettelman acknowledges funding from the NSF OPP grant #1744946. K.
594 Zhang and J. Sun acknowledges support from the Energy Exascale Earth System Model project.
595 The Pacific Northwest National Laboratory is operated for the U.S. DOE by Battelle Memorial

596 Institute under contract DE-AC05-76RL01830. We acknowledge the support from the
597 NCAR/Earth Observing Laboratory pilots, technicians, and flight crews for the NSF SOCRATES
598 flight campaign. NCAR is sponsored by the National Science Foundation. M. Diao provided
599 laboratory calibrations and QA/QC of the VCSEL hygrometer and S. Beaton contributed to the
600 field support. All aircraft observations can be obtained at <https://data.eol.ucar.edu/>.

601 **References**

- 602 Bergeron, T. (1928). Über die dreidimensional verknüpfende Wetteranalyse. *Geophys. Norv.*,
603 5(7), 1–111. [https://doi.org/10.1175/1520-0493\(1931\)59<275:TBBDDV>2.0.CO;2](https://doi.org/10.1175/1520-0493(1931)59<275:TBBDDV>2.0.CO;2)
- 604 Bodas-Salcedo, A., Hill, P. G., Furtado, K., Williams, K. D., Field, P. R., Manners, J. C., et al.
605 (2016). Large Contribution of Supercooled Liquid Clouds to the Solar Radiation Budget of
606 the Southern Ocean. *J. Climate*, 29, 4213–4228. <https://doi.org/10.1175/JCLI-D-15-0564.1>
- 607 Borys, R. D., Lowenthal, D. H., Cohn, S. A., & Brown, W. O. J. (2003). Mountaintop and radar
608 measurements of anthropogenic aerosol effects on snow growth and snowfall rate.
609 *Geophysical Research Letters*, 30(10). <https://doi.org/10.1029/2002gl016855>
- 610 Bühl, J., Seifert, P., Engelmann, R., & Ansmann, A. (2019). Impact of vertical air motions on ice
611 formation rate in mixed-phase cloud layers. *npj Clim Atmos Sci*, 2(36)
612 <https://doi.org/10.1038/s41612-019-0092-6>
- 613 Chen, T., Rossow, W. B., & Zhang, Y. (2000). Radiative Effects of Cloud-Type Variations. *J.*
614 *Climate*, 13(264–286). [https://doi.org/10.1175/1520-](https://doi.org/10.1175/1520-0442(2000)013<0264:REOCTV>2.0.CO;2)
615 [0442\(2000\)013<0264:REOCTV>2.0.CO;2](https://doi.org/10.1175/1520-0442(2000)013<0264:REOCTV>2.0.CO;2)
- 616 D’Alessandro, J. J., Diao, M., Wu, C., Liu, X., Jensen, J. B., & Stephens, B. B. (2019). Cloud
617 phase and relative humidity distributions over the Southern Ocean in austral summer based
618 on in situ observations and CAM5 simulations. *Journal of Climate*, 32(10), 2781–2805.
619 <https://doi.org/10.1175/JCLI-D-18-0232.1>

620 DeMott, P. J., Prenni, A. J., Liu, X., Kreidenweis, S. M., Petters, M. D., Twohy, C. H., et al.
621 (2010). Predicting global atmospheric ice nuclei distributions and their impacts on climate.
622 *Proceedings of the National Academy of Sciences of the United States of America*, 107(25),
623 11217–11222. <https://doi.org/10.1073/pnas.0910818107>

624 Diao, M. (2020). VCSEL 1 Hz Water Vapor Data. *UCAR/NCAR - Earth Observing Laboratory*.
625 <https://doi.org/10.26023/KFSD-Y8DQ-YC0D>, <https://data.eol.ucar.edu/dataset/552.051>

626 Eidhammer, T., Morrison, H., Bansemer, A., Gettelman, A., & Heymsfield, A. J. (2014).
627 Comparison of ice cloud properties simulated by the Community Atmosphere Model
628 (CAM5) with in-situ observations. *Atmos. Chem. Phys*, 14, 10103–10118.
629 <https://doi.org/10.5194/acp-14-10103-2014>

630 Fan, J., Ghan, S., Ovchinnikov, M., Liu, X., Rasch, P. J., & Korolev, A. (2011). Representation
631 of Arctic mixed-phase clouds and the Wegener-Bergeron-Findeisen process in climate
632 models: Perspectives from a cloud-resolving study. *Journal of Geophysical Research*,
633 116(D00T07). <https://doi.org/10.1029/2010JD015375>

634 Gettelman, A., & Morrison, H. (2015). Advanced two-moment bulk microphysics for global
635 models. Part I: Off-line tests and comparison with other schemes. *Journal of Climate*, 28(3),
636 1268–1287. <https://doi.org/10.1175/JCLI-D-14-00102.1>

637 Gettelman, A., Bardeen, C., McCluskey, C. S., Järvinen, E. J., Stith, J., Bretherton, C.,
638 McFarquhar, G., Twohy, C., D’Alessandro, J., & Wu, W. (2020) Simulating Observations
639 of Southern Ocean Clouds and Implications for Climate. *Journal of Geophysical Research*.
640 In press.

641 Gierens, R., Kneifel, S., Shupe, M. D., Ebell, K., Maturilli, M., & Löhnert, U. (2020). Low-level
642 mixed-phase clouds in a complex Arctic environment. *Atmospheric Chemistry and Physics*,
643 *20*(6), 3459–3481. <https://doi.org/10.5194/acp-20-3459-2020>

644 Guo, Z., Wang, M., Peng, Y., & Luo, Y. (2020). Evaluation on the Vertical Distribution of
645 Liquid and Ice Phase Cloud Fraction in Community Atmosphere Model Version 5.3 using
646 Spaceborne Lidar Observations. *Earth and Space Science*, *7*, e2019EA001029,
647 <https://doi.org/10.1029/2019EA001029>

648 Hallett, J., & Mossop, S. C. (1974). Production of secondary ice particles during the riming
649 process. *Nature*, *249*(5452), 26–28. <https://doi.org/10.1038/249026a0>

650 Jackson, R. C., McFarquhar, G. M., Korolev, A. V., Earle, M. E., Liu, P. S. K., Lawson, R. P., et
651 al. (2012). The dependence of ice microphysics on aerosol concentration in arctic mixed-
652 phase stratus clouds during ISDAC and M-PACE. *Journal of Geophysical Research:*
653 *Atmospheres*, *117*, D15207, <https://doi.org/10.1029/2012JD017668>

654 Kay, J. E., Hillman, B. R., Klein, S. A., Zhang, Y., Medeiros, B., Pincus, R., et al. (2012).
655 Exposing Global Cloud Biases in the Community Atmosphere Model (CAM) Using
656 Satellite Observations and Their Corresponding Instrument Simulators. *J. Climate*, *25*(15),
657 5190–5207. <https://doi.org/10.1175/JCLI-D-11-00469.1>

658 Kay, J. E., Wall, C., Yettella, V., Medeiros, B., Hannay, C., Caldwell, P., & Bitz, C. (2016).
659 Global Climate Impacts of Fixing the Southern Ocean Shortwave Radiation Bias in the
660 Community Earth System Model (CESM). *Journal of Climate*, *29*(12), 4617–4636.
661 <https://doi.org/10.1175/JCLI-D-15-0358.1>

662 Klein, S. A., McCoy, R. B., Morrison, H., Ackerman, A. S., Avramov, A., De Boer, G., et al.
663 (2009). Intercomparison of model simulations of mixed-phase clouds observed during the
664 ARM Mixed-Phase Arctic Cloud Experiment. I: Single-layer cloud. *Q. J. R. Meteorol. Soc.*,
665 *135*, 979–1002. <https://doi.org/10.1002/qj.416>

666 Korolev, A., McFarquhar, G., Field, P. R., Franklin, C., Lawson, P., Wang, Z., et al. (2017).
667 Mixed-Phase Clouds: Progress and Challenges. *Meteorological Monographs*, *58*, 5.1-5.50.
668 <https://doi.org/10.1175/amsmonographs-d-17-0001.1>

669 Korolev, A., & Isaac, G. (2003). Phase transformation of mixed-phase clouds. *Quarterly Journal*
670 *of the Royal Meteorological Society*, *129*(587), 19–38. <https://doi.org/10.1256/qj.01.203>

671 Korolev, A., & Isaac, G. A. (2006). Relative humidity in liquid, mixed-phase, and ice clouds.
672 *Journal of the Atmospheric Sciences*, *63*(11), 2865–2880.
673 <https://doi.org/10.1175/JAS3784.1>

674 Korolev, A., & Field, P. R. (2008). The Effect of Dynamics on Mixed-Phase Clouds: Theoretical
675 Considerations. *J. Atmos. Sci.*, *65*, 66–86, <https://doi.org/10.1175/2007JAS2355.1>

676 Lin, S.-J. (2004). A “Vertically Lagrangian” Finite-Volume Dynamical Core for Global Models.
677 *Mon. Wea. Rev.*, *132*, 2293–2307. [https://doi.org/10.1175/1520-](https://doi.org/10.1175/1520-0493(2004)132<2293:AVLFDC>2.0.CO;2)
678 [0493\(2004\)132<2293:AVLFDC>2.0.CO;2](https://doi.org/10.1175/1520-0493(2004)132<2293:AVLFDC>2.0.CO;2)

679 Liou, K. N. (1992), *Radiation and Cloud Processes in the Atmosphere*, pp. 255–339, Oxford
680 Univ. Press, New York.

681 Liu, X., Easter, R. C., Ghan, S. J., Zaveri, R., Rasch, P., Shi, X., et al. (2012). Toward a minimal
682 representation of aerosols in climate models: Description and evaluation in the Community
683 Atmosphere Model CAM5. *Geoscientific Model Development*, 5(3), 709–739.
684 <https://doi.org/10.5194/gmd-5-709-2012>

685 Liu, X., Ma, P. L., Wang, H., Tilmes, S., Singh, B., Easter, R. C., et al. (2016). Description and
686 evaluation of a new four-mode version of the Modal Aerosol Module (MAM4) within
687 version 5.3 of the Community Atmosphere Model. *Geoscientific Model Development*, 9(2),
688 505–522. <https://doi.org/10.5194/gmd-9-505-2016>

689 Lohmann, U., Henneberger, J., Henneberg, O., Fugal, J. P., Bühl, J., & Kanji, Z. A. (2016).
690 Persistence of orographic mixed-phase clouds. *Geophysical Research Letters*, 43(19),
691 10,512–10,519. <https://doi.org/10.1002/2016GL071036>

692 Lohmann, U. (2002). Possible Aerosol Effects on Ice Clouds via Contact Nucleation. *J. Atmos.*
693 *Sci.*, 59, 647–656, [https://doi.org/10.1175/1520-0469\(2001\)059<0647:PAEOIC>2.0.CO;2](https://doi.org/10.1175/1520-0469(2001)059<0647:PAEOIC>2.0.CO;2)

694 Matus, A. V., & L'Ecuyer, T. S. (2017). The role of cloud phase in Earth's radiation budget.
695 *Journal of Geophysical Research: Atmospheres*, 122(5), 2559–2578.
696 <https://doi.org/10.1002/2016JD025951>

697 McCoy, D. T., Tan, I., Hartmann, D. L., Zelinka, M. D., & Storelvmo, T. (2016). On the
698 relationships among cloud cover, mixed-phase partitioning, and planetary albedo in GCMs.
699 *Journal of Advances in Modeling Earth Systems*, 8(2), 650–668.
700 <https://doi.org/10.1002/2015MS000589>

701 Morrison, A. E., Siems, S. T., Manton, M. J., & Nazarov, A. (2010). A modeling case study of
702 mixed-phase clouds over the Southern Ocean and Tasmania. *Monthly Weather Review*,
703 *138*(3), 839–862. <https://doi.org/10.1175/2009MWR3011.1>

704 Morrison, H., & Gettelman, A. (2008). A New Two-Moment Bulk Stratiform Cloud
705 Microphysics Scheme in the Community Atmosphere Model, Version 3 (CAM3). Part I:
706 Description and Numerical Tests. *J. Climate*, *21*(15), 3642–3659.
707 <https://doi.org/10.1175/2008JCLI2105.1>

708 Mülmenstädt, J., Sourdeval, O., Delanoë, J., & Quaas, J. (2015). Frequency of occurrence of rain
709 from liquid-, mixed-, and ice-phase clouds derived from A-Train satellite retrievals.
710 *Geophysical Research Letters*, *42*(15), 6502–6509. <https://doi.org/10.1002/2015GL064604>

711 Murphy, D. M., & Koop, T. (2005). Review of the vapour pressures of ice and supercooled water
712 for atmospheric applications. *Quarterly Journal of the Royal Meteorological Society*,
713 *131*(608), 1539–1565. <https://doi.org/10.1256/qj.04.94>

714 Neale, R. B., Chen, C.-C., Gettelman, A., Lauritzen, P. H., Park, S., Williamson, D. L., et al.
715 (2012). *Description of the NCAR Community Atmosphere Model (CAM 5.0)*. NCAR Tech
716 Note TN-486, 268 pp.

717 Park, S., & Bretherton, C. S. (2009). The University of Washington shallow convection and
718 moist turbulence schemes and their impact on climate simulations with the community
719 atmosphere model. *Journal of Climate*, *22*(12), 3449–3469.
720 <https://doi.org/10.1175/2008JCLI2557.1>

721 Patnaude, R., Diao, M., Liu, X., & Chu, S. (2020). Effects of Thermodynamics, Dynamics and
722 Aerosols on Cirrus Clouds Based on In Situ Observations and NCAR CAM6 Model. *Atmos.*
723 *Chem. Phys. Discuss.*, <https://doi.org/10.5194/acp-2020-497>

724 Qiu, S., Xi, B., & Dong, X. (2018). Influence of Wind Direction on Thermodynamic Properties
725 and Arctic Mixed-Phase Clouds in Autumn at Utqiagvik, Alaska. *Journal of Geophysical*
726 *Research: Atmospheres*, *123*(17), 9589–9603. <https://doi.org/10.1029/2018JD028631>

727 Rangno, A. L., & Hobbs, P. V. (2001). Ice particles in stratiform clouds in the Arctic and
728 possible mechanisms for the production of high ice concentrations. *Journal of Geophysical*
729 *Research: Atmospheres*, *106*(D14), 15065–15075. <https://doi.org/10.1029/2000JD900286>

730 Rasch, P. J., Xie, S., Ma, P. -L., Lin, W., Wang, H., Tang, Q., et al. (2019). An Overview of the
731 Atmospheric Component of the Energy Exascale Earth System Model. *Journal of Advances*
732 *in Modeling Earth Systems*, *11*(8), 2377–2411. <https://doi.org/10.1029/2019MS001629>

733 Shupe, M. D., Kollias, P., Persson, P. O. G., & McFarquhar, G. M. (2008). Vertical Motions in
734 Arctic Mixed-Phase Stratiform Clouds. *J. Atmos. Sci.*, *65*, 1304–1322,
735 <https://doi.org/10.1175/2007JAS2479.1>

736 Storelvmo, T., Hoose, C., & Eriksson, P. (2011). Global modeling of mixed-phase clouds: The
737 albedo and lifetime effects of aerosols. *Journal of Geophysical Research*, *116*(D5), D05207.
738 <https://doi.org/10.1029/2010JD014724>

739 Sun, J., Zhang, K., Wan, H., Ma, P., Tang, Q., & Zhang, S. (2019). Impact of Nudging Strategy
740 on the Climate Representativeness and Hindcast Skill of Constrained EAMv1 Simulations.
741 *Journal of Advances in Modeling Earth Systems*, *11*(12), 3911–3933.

742 <https://doi.org/10.1029/2019MS001831>

743 Tan, I., & Storelvmo, T. (2016). Sensitivity study on the influence of cloud microphysical
744 parameters on mixed-phase cloud thermodynamic phase partitioning in CAM5. *Journal of*
745 *the Atmospheric Sciences*, 73(2), 709–728. <https://doi.org/10.1175/JAS-D-15-0152.1>

746 Tan, I., Storelvmo, T., & Zelinka, M. D. (2016). Observational constraints on mixed-phase
747 clouds imply higher climate sensitivity. *Science*, 352, 224–227,
748 <https://doi.org/10.1126/science.aad5300>

749 Trenberth, K. E., & Fasullo, J. T. (2010). Simulation of present-day and twenty-first-century
750 energy budgets of the southern oceans. *Journal of Climate*, 23(2), 440–454.
751 <https://doi.org/10.1175/2009JCLI3152.1>

752 Wegener, A. (1912). Thermodynamik der Atmosphäre. *Nature*, 90(2237), 31–31.
753 <https://doi.org/10.1038/090031a0>

754 Williams, K. D., Bodas-Salcedo, A., Dé Qué, M., Fermepin, S., Medeiros, B., Watanabe, M., et
755 al. (2013). The Transpose-AMIP II Experiment and Its Application to the Understanding of
756 Southern Ocean Cloud Biases in Climate Models. *J. Climate*, 26, 3258–3274.
757 <https://doi.org/10.1175/JCLI-D-12-00429.1>

758 Wu, C., Liu, X., Diao, M., Zhang, K., Gettelman, A., Lu, Z., Penner, J. E., & Lin, Z. (2017).
759 Direct comparisons of ice cloud macro- and microphysical properties simulated by the
760 Community Atmosphere Model version 5 with HIPPO aircraft observations. *Atmos. Chem.*
761 *Phys.*, 17, 4731–4749, <https://doi.org/10.5194/acp-17-4731-2017>.

762 Zhang, D., Vogelmann, A., Kollias, P., Luke, E., Yang, F., Lubin, D., & Wang, Z. (2019).
763 Comparison of Antarctic and Arctic Single-Layer Stratiform Mixed-Phase Cloud Properties
764 Using Ground-Based Remote Sensing Measurements. *Journal of Geophysical Research:*
765 *Atmospheres*, 124(17–18), 10186–10204. <https://doi.org/10.1029/2019JD030673>

766 Zhang, M., Liu, X., Diao, M., D’Alessandro, J. J., Wang, Y., Wu, C., et al. (2019). Impacts of
767 Representing Heterogeneous Distribution of Cloud Liquid and Ice on Phase Partitioning of
768 Arctic Mixed-Phase Clouds with NCAR CAM5. *Journal of Geophysical Research:*
769 *Atmospheres*, 124(23), 13071–13090. <https://doi.org/10.1029/2019JD030502>

770 Zhang, Y., Xie, S., Lin, W., Klein, S. A., Zelinka, M., Ma, P., et al. (2019). Evaluation of Clouds
771 in Version 1 of the E3SM Atmosphere Model With Satellite Simulators. *Journal of*
772 *Advances in Modeling Earth Systems*, 11(5), 1253–1268.
773 <https://doi.org/10.1029/2018MS001562>

774 Zhang, M., Xie, S., Liu, X., Lin, W., Zhang, K., Ma, H., et al. (2020). Toward Understanding the
775 Simulated Phase Partitioning of Arctic Single-Layer Mixed-Phase Clouds in E3SM. *Earth*
776 *and Space Science*, 7(7). <https://doi.org/10.1029/2020ea001125>

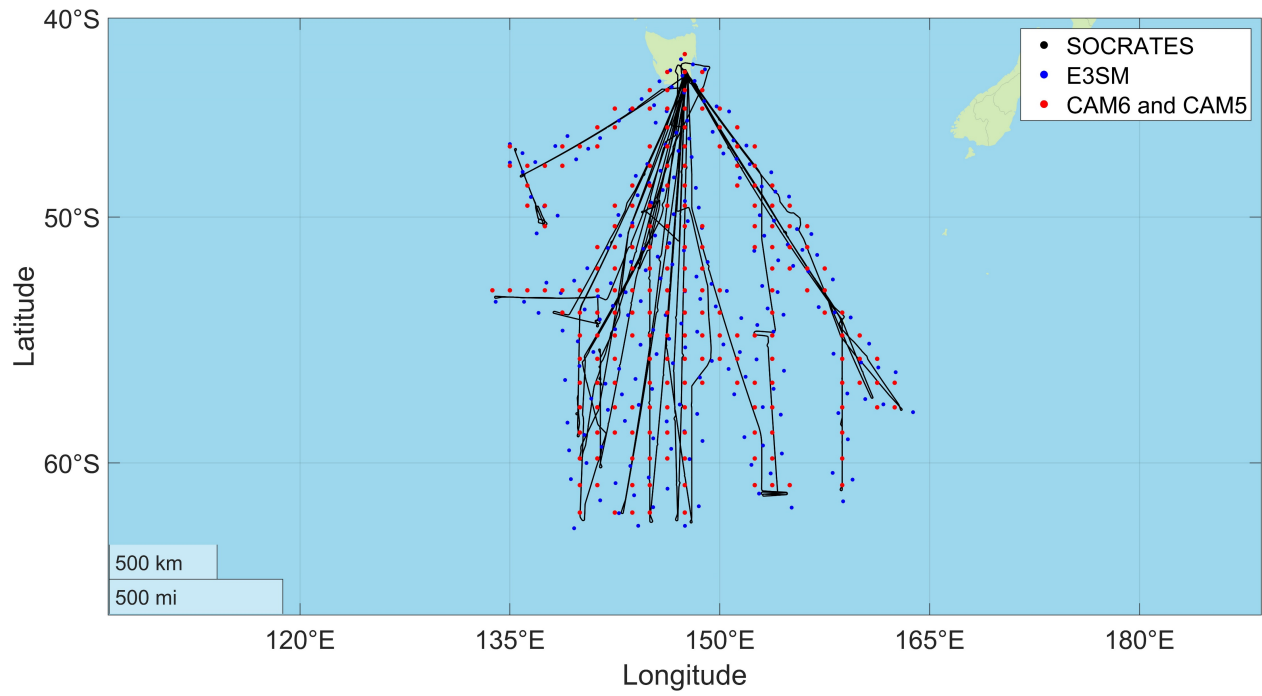
777 Zondlo, M. A., Paige, M. E., Massick, S. M., & Silver, J. A. (2010). Vertical cavity laser
778 hygrometer for the National Science Foundation Gulfstream-V aircraft. *Journal of*
779 *Geophysical Research*, 115(D20), D20309. <https://doi.org/10.1029/2010JD014445>

780

781 Table 1. The maximum and minimum values of thermodynamic conditions and cloud
 782 microphysical properties used in this study for observations and simulations.

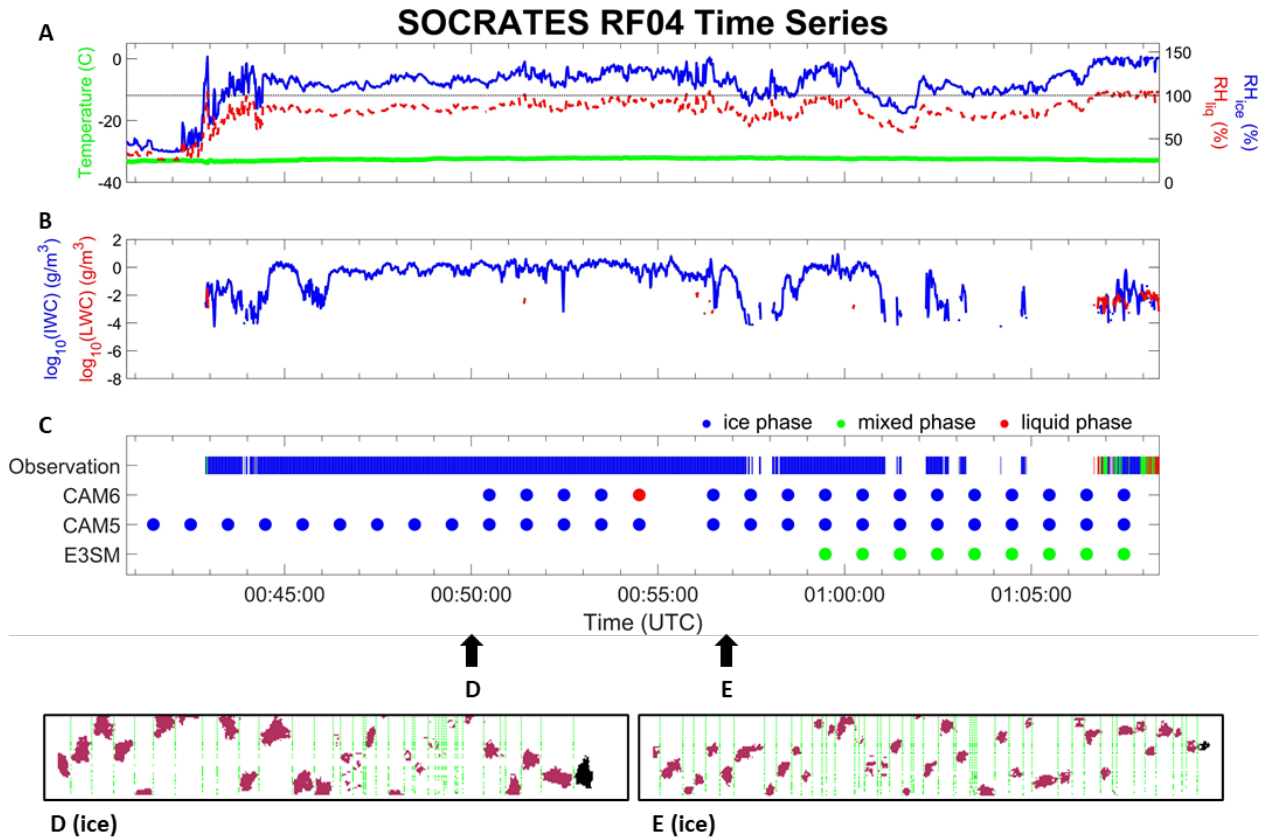
Variables	1-s observations	200-s observations	580-s observations	CAM6	CAM5	E3SM
T (°C)	-39.7 – 0.0	-39.7 – 0.0	-39.7 – 0.0	-37.6 – 0.0	-37.4 – 0.0	-38.5 – 0.0
P (Pa)	37,623 – 96,848	37,644 – 97,131	37,645 – 96,958	32,207 – 96,777	32,212 – 98,315	32,760 – 102,116
LWC (g m ⁻³)	5.01×10 ⁻⁵ – 1.41	2.76×10 ⁻⁷ – 0.66	9.52×10 ⁻⁸ – 0.53	1.26×10 ⁻⁵ – 0.36	1.26×10 ⁻⁷ – 0.30	1.41×10 ⁻⁷ – 0.34
IWC (g m ⁻³)	5.68×10 ⁻⁵ – 55.8	3.79×10 ⁻⁷ – 13.9	1.31×10 ⁻⁷ – 7.73	1.09×10 ⁻⁷ – 0.14	3.17×10 ⁻⁷ – 0.18	1.13×10 ⁻⁷ – 0.18
N _{liq} (cm ⁻³)	4.87×10 ⁻⁵ – 564.85	2.59×10 ⁻⁷ – 218.00	9.16×10 ⁻⁸ – 210.56	5.01×10 ⁻⁴ – 86.85	1.41×10 ⁻⁷ – 185.70	1.02×10 ⁻⁷ – 85.53
N _{ice} (cm ⁻³)	4.83×10 ⁻⁵ – 0.47	2.45×10 ⁻⁷ – 0.07	8.62×10 ⁻⁸ – 0.04	2.77×10 ⁻⁶ – 0.08	5.34×10 ⁻⁶ – 15.14	1.53×10 ⁻⁷ – 9.71
In-cloud RH _{liq} (%)	3.7 – 105.0	3.9 – 102.3	6.8 – 101.7	23.2 – 101.3	42.3 – 99.5	55.8 – 104.5
In-cloud RH _{ice} (%)	4.3 – 146.7	4.1 – 137.3	8.0 – 126.8	25.3 – 133.8	52.1 – 115.8	65.5 – 143.8
Clear-sky RH _{liq} (%)	1.1 – 104.8	1.7 – 93.1	2.0 – 88.8	5.3 – 97.6	5.4 – 97.0	0.0 – 98.8
Clear-sky RH _{ice} (%)	1.1 – 141.8	2.0 – 117.7	2.3 – 109.2	6.3 – 110.9	6.5 – 103.6	0.0 – 125.0

783



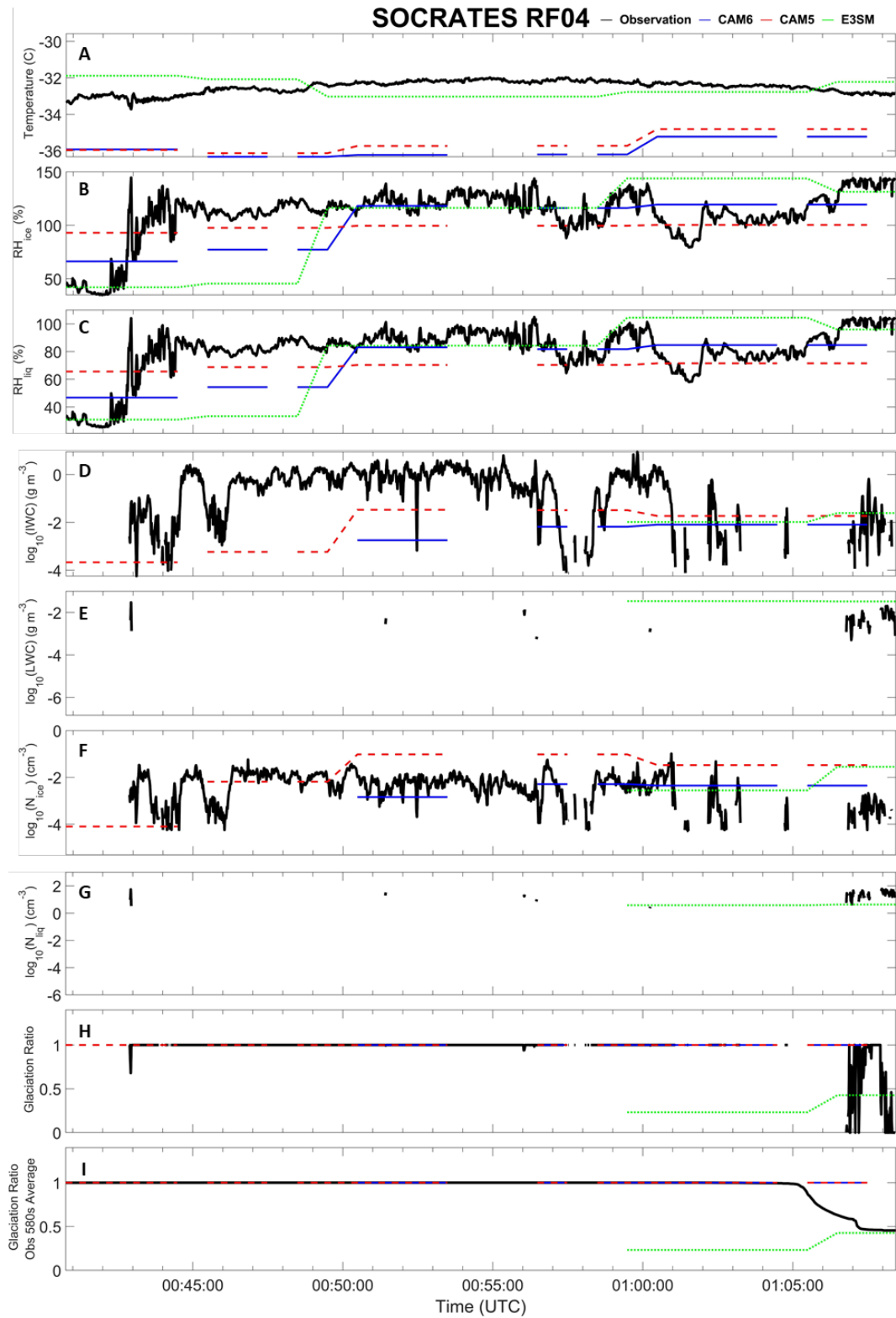
784

785 Figure 1. Flight tracks of a total 15 research flights in the NSF SOCRATES campaign (black) and
 786 the collocated grid coordinates for CAM6 (red), CAM5 (red) and E3SM (blue) simulations.



787

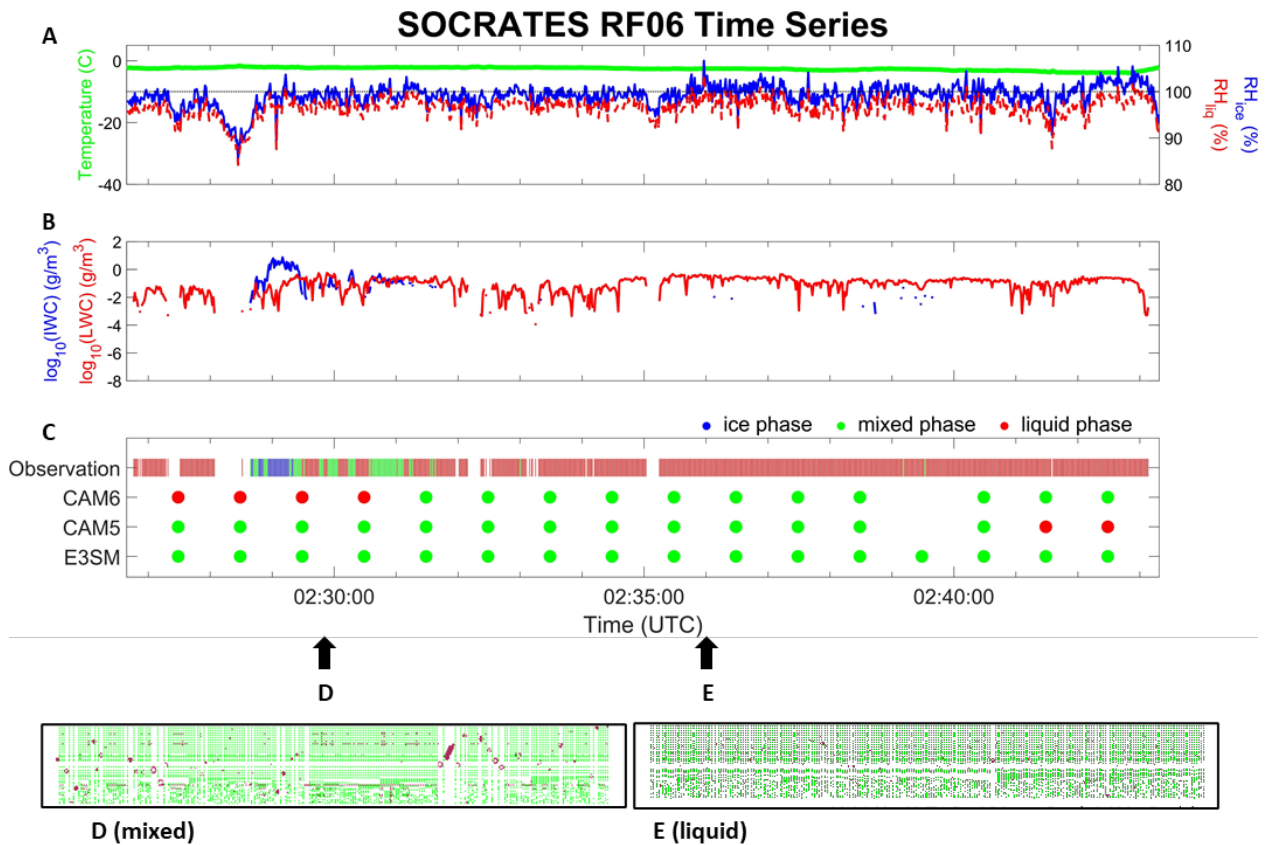
788 Figure 2. An example time series of ice-phase dominated clouds in NSF SOCRATES campaign
 789 Research Flight 4 (RF04). (a) 1-Hz observations of temperature (green), RH_{ice} (blue), RH_{liq} (red),
 790 and $RH = 100\%$ (dashed black). (b) 1-Hz observations of log-scale IWC (blue) and LWC (red). (c)
 791 Cloud phases identified from the 1-Hz observations (vertical bars) and simulated by the CAM6,
 792 CAM5, and E3SM (dots). (d) and (e) illustrate the seconds of ice cloud particle imageries captured
 793 by the Fast-2DC probe.



794

795 Figure 3. Time series for the same time interval of RF04 in Figure 2, compared between
 796 observations and simulations, including (a) temperature, (b) RH_{ice} (c) RH_{liq} , (d) $\log_{10}(IWC)$, (e)

797 $\log_{10}(\text{LWC})$, (f) N_{ice} , (g) N_{liq} , (h) glaciation ratio, and (i) glaciation ratio using 580-second
798 averaged observations. (a) to (h) are based on 1-Hz observations. Colored lines represent
799 observations (black), CAM6 (blue), CAM5 (red), and E3SM (green).

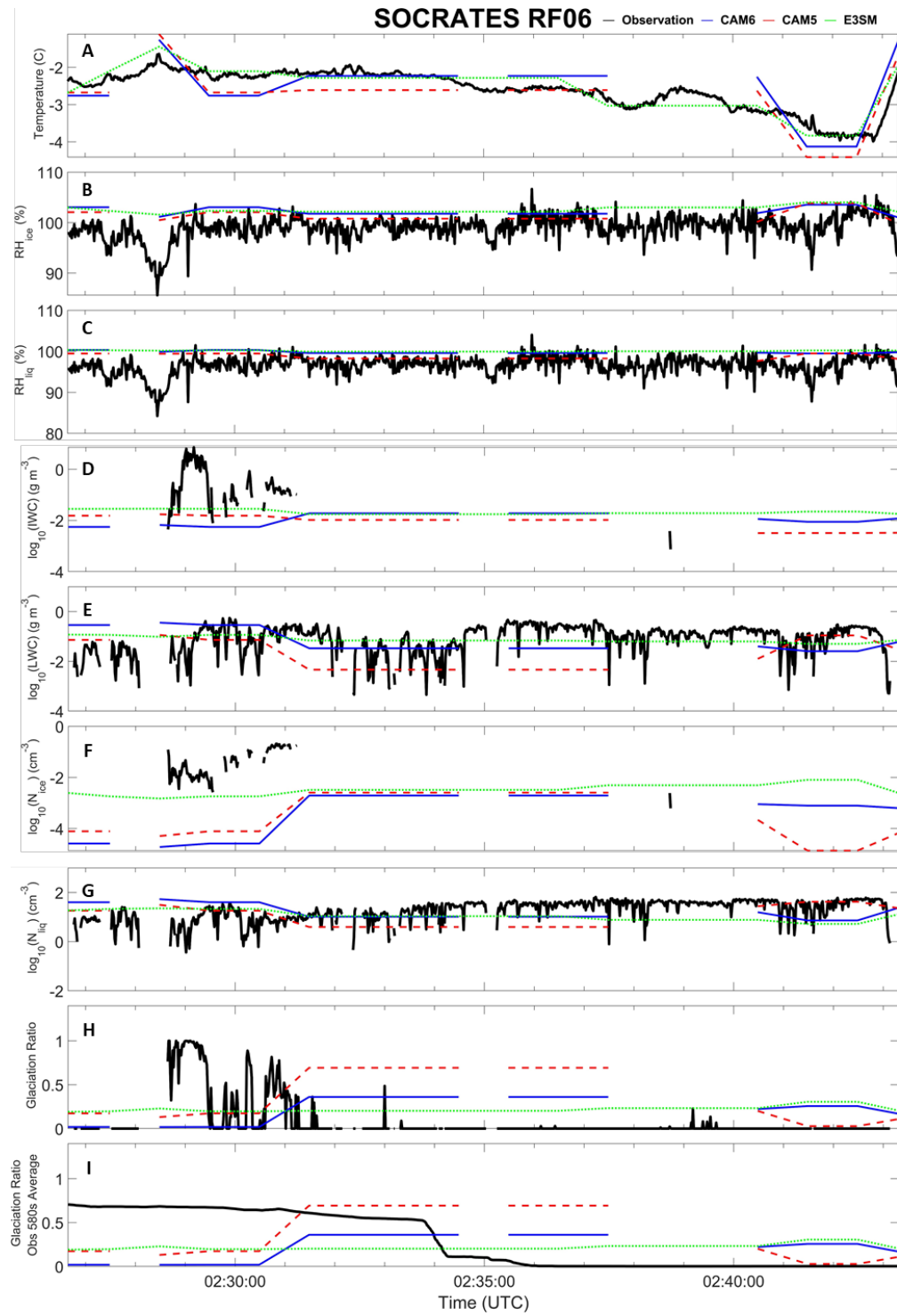


800

801 Figure 4. Similar to Figure 2 but for liquid-phase dominated clouds in Research Flight 6 (RF06).

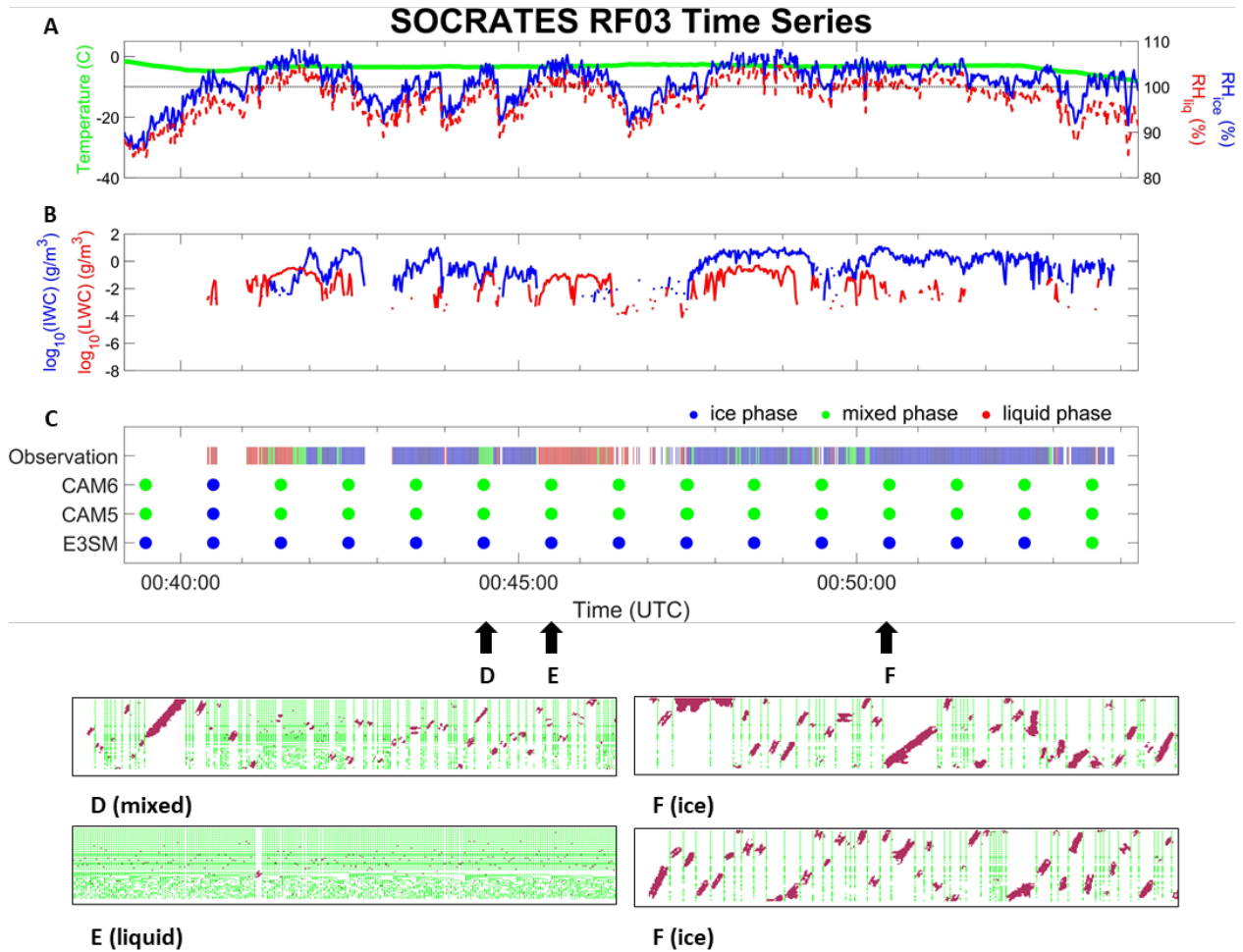
802 In (d) and (e), individual seconds of mixed phase and liquid phase cloud particle imageries are

803 captured, respectively.



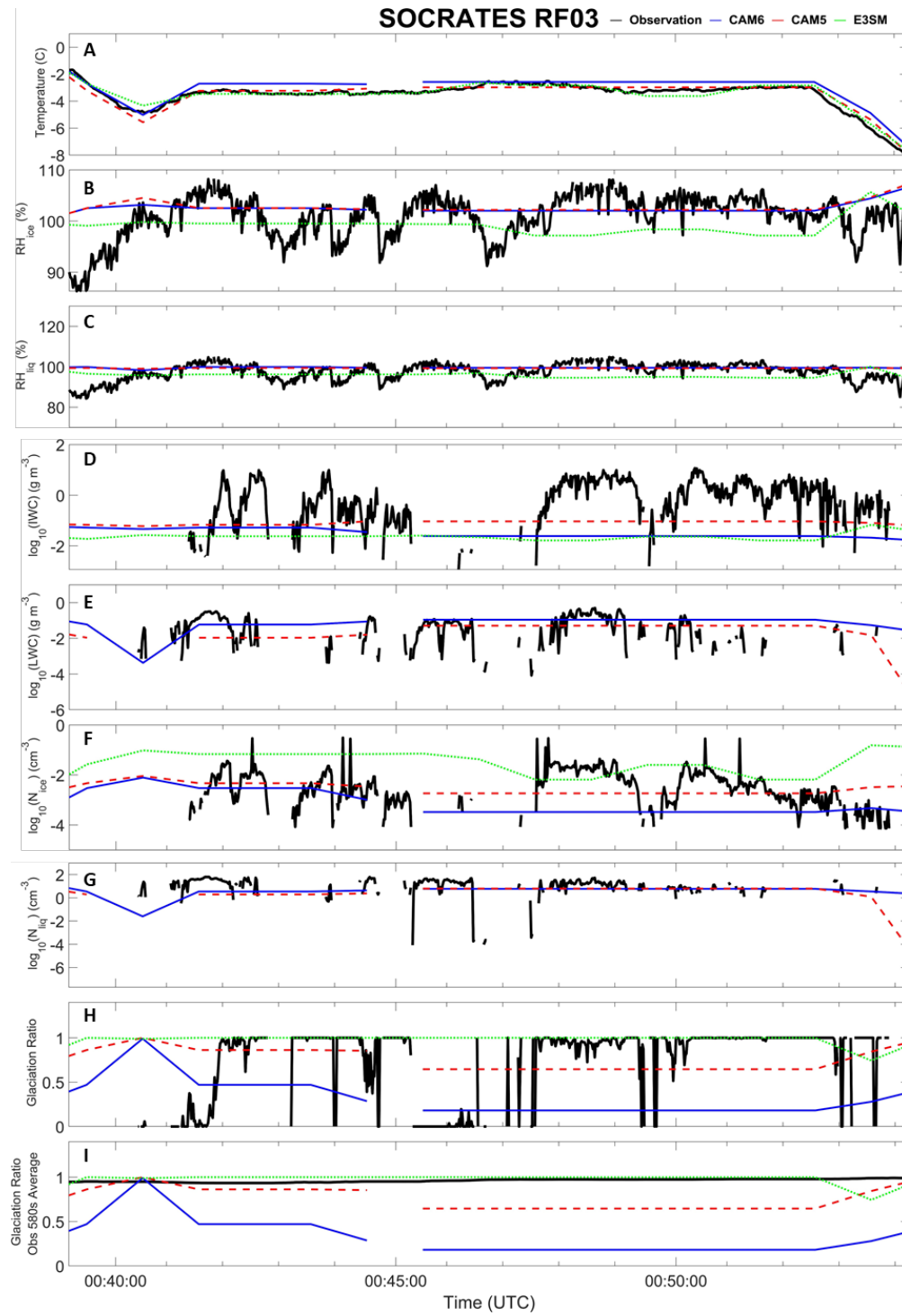
804

805 Figure 5. Similar to Figure 3 but for RF06.



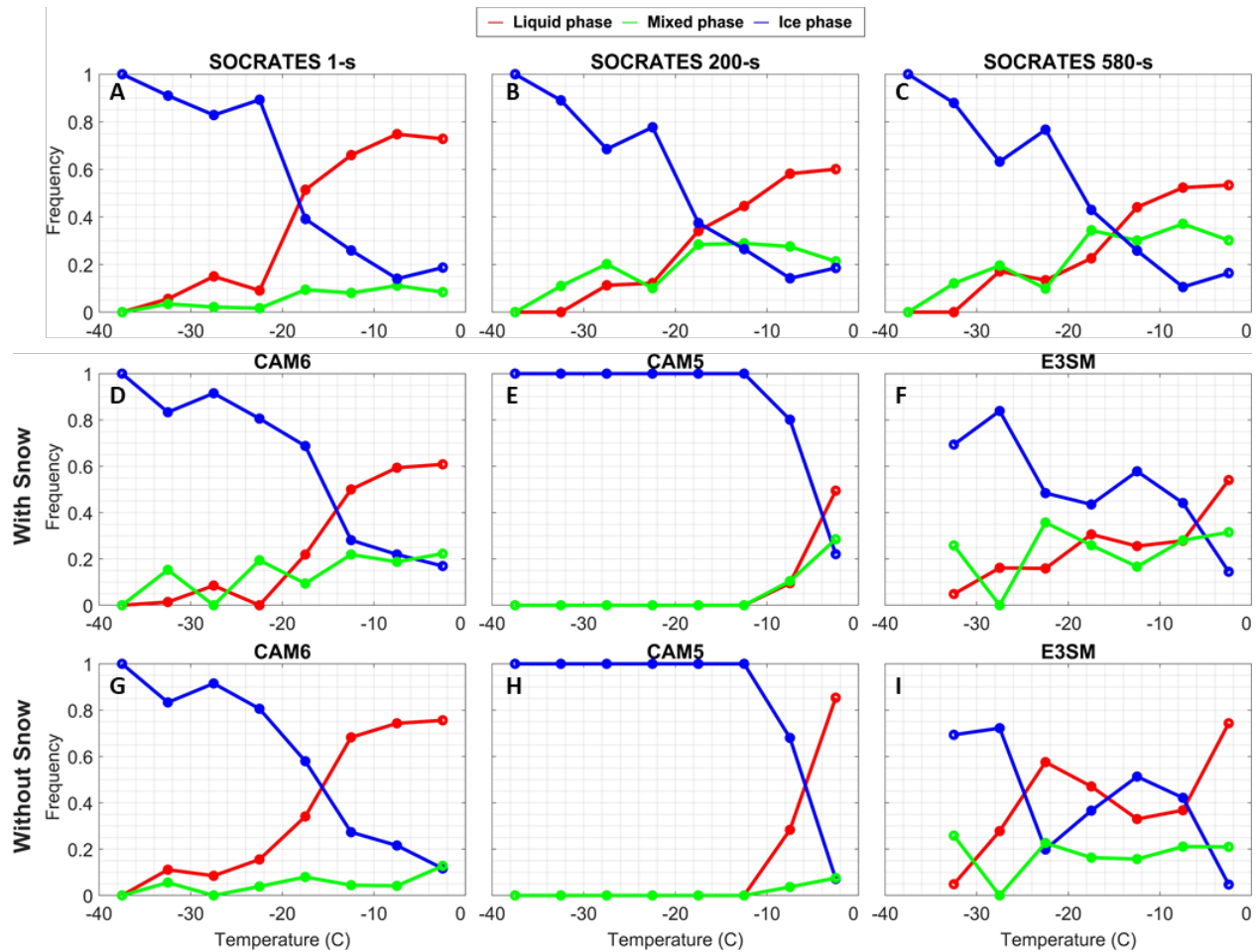
806

807 Figure 6. Similar to Figure 2 but for a case of spatially heterogeneous clouds with three phases in
 808 Research Flight 3 (RF03). Individual seconds of mixed phase, liquid phase, and ice phase cloud
 809 particle imageries are noted by (d), (e), and (f), respectively.



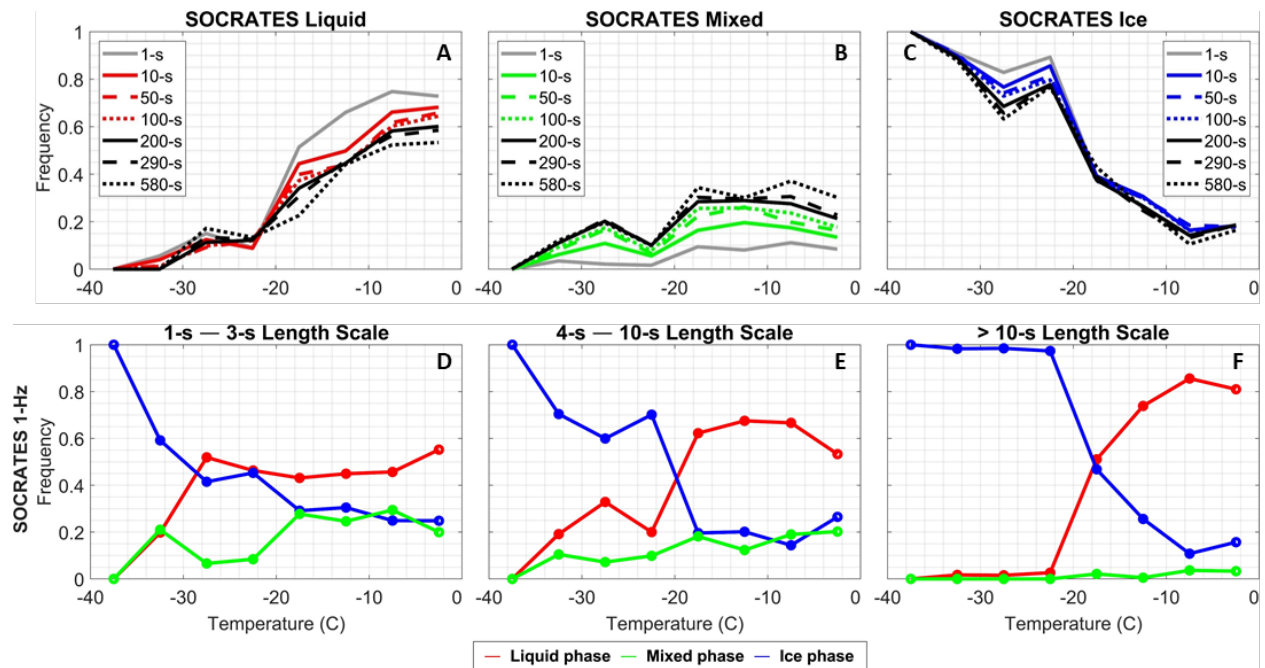
810

811 Figure 7. Similar to Figure 3 but for RF03.



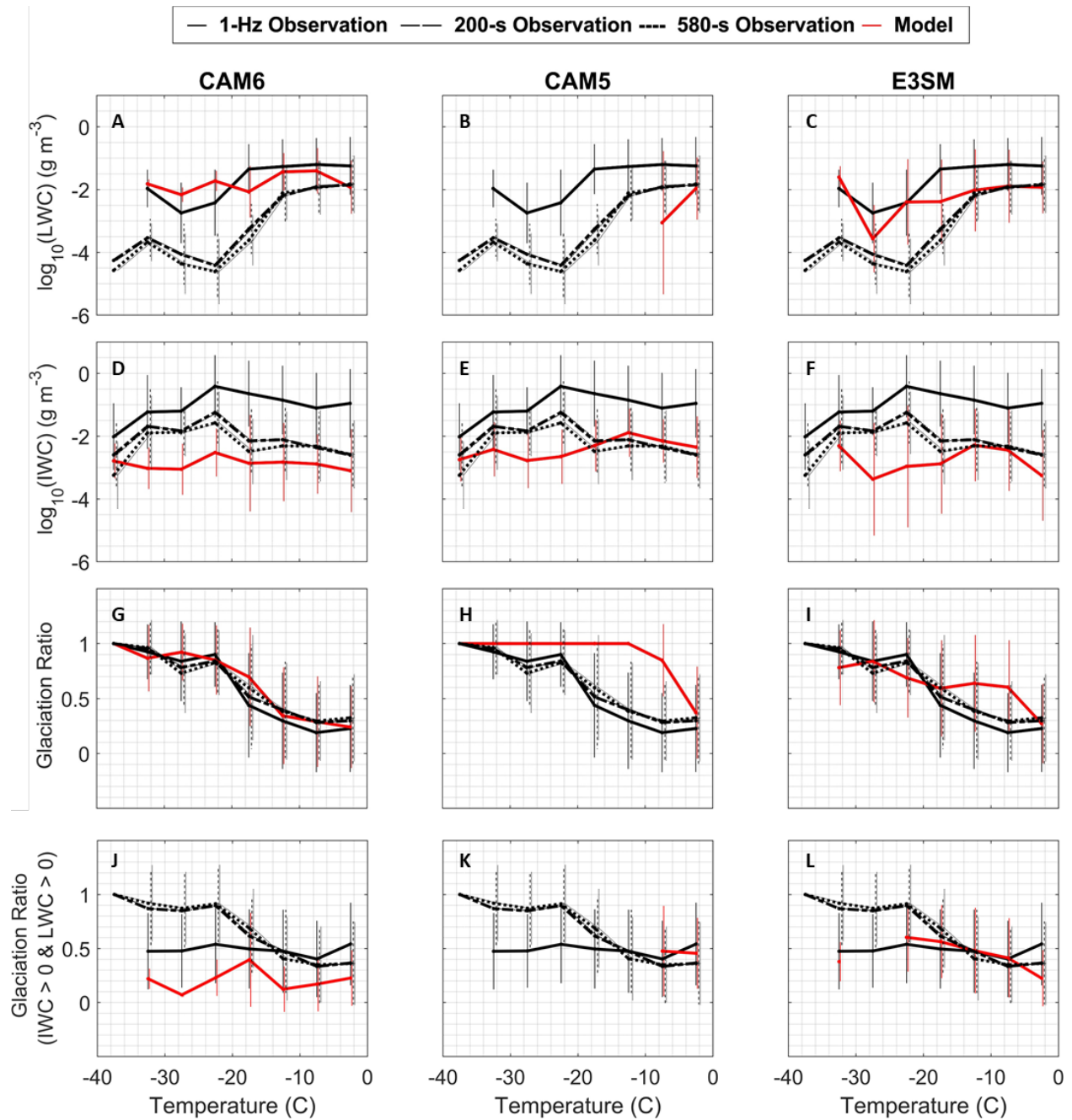
812

813 Figure 8. Cloud phase occurrence frequencies for (a) 1-Hz SOCRATES observations, (b) 200-s
 814 averaged observations, and (c) 580-s averaged observations with temperature ranged from -40°C
 815 to 0°C, binned by 5°C. Cloud phase occurrence frequencies for CAM6, CAM5, and E3SM are
 816 shown for two types of simulated IWC: (d – f) including snow and (g – i) excluding snow. Liquid,
 817 mixed, and ice phase are denoted by red, green, and blue colors, respectively.



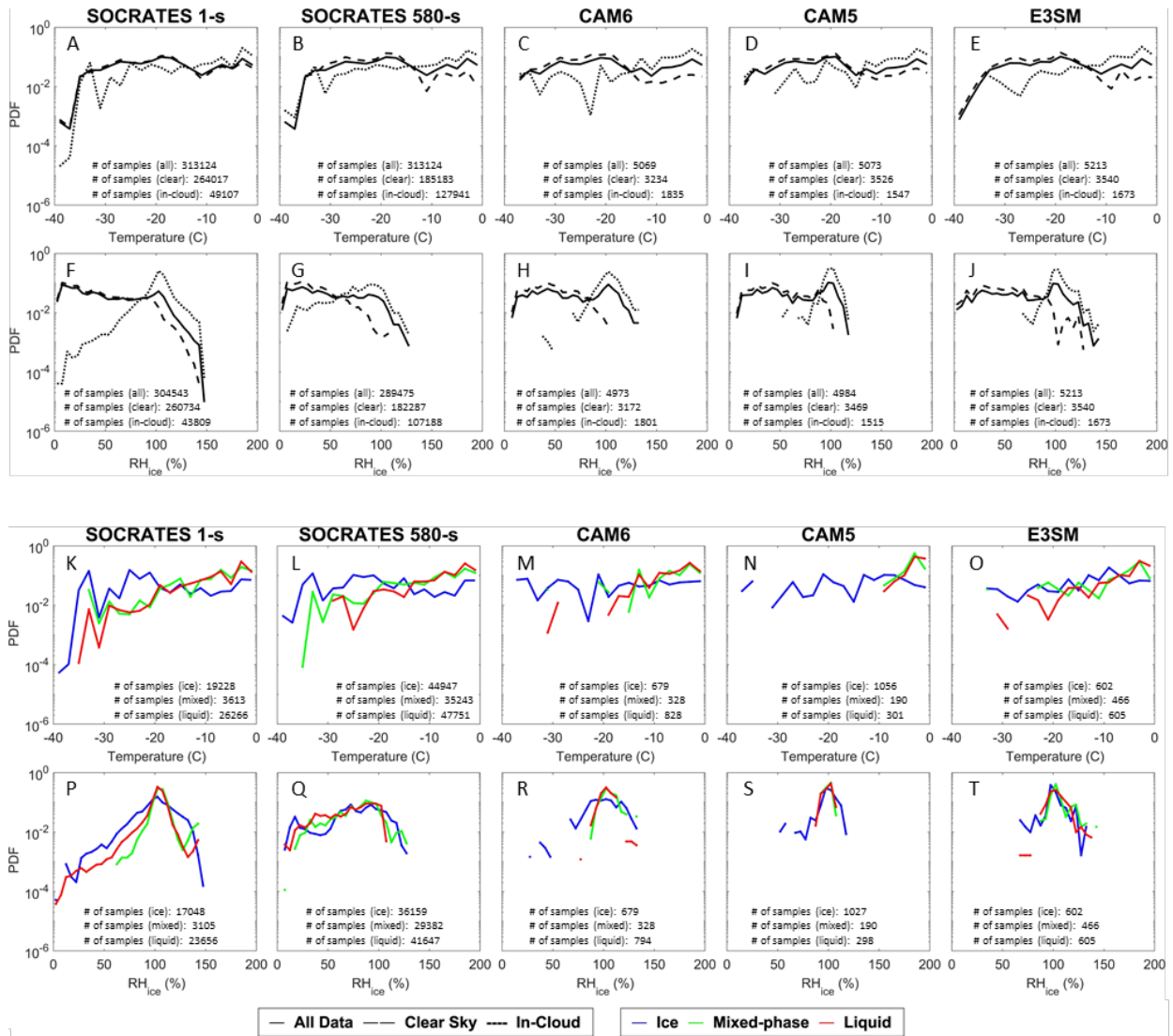
818

819 Figure 9. Cloud phase occurrence frequencies for (a) liquid phase, (b) mixed phase, and (c) ice
 820 phase are shown for 1-s, 10-s, 50-s, 100-s, 200-s, 290-s, and 580-s averaged observations. (d – f)
 821 Occurrence frequency of various length scales of cloud phase, calculated based on 1-Hz
 822 observations, including (d) 1-s – 3-s length scale, (e) 4-s – 10-s length scale, and (f) more than
 823 10-s length scale.



824

825 Figure 10. Averages and standard deviations of (a – c) log-scale LWC, (d – f) log-scale IWC, (g –
 826 i) glaciation ratio (i.e., IWC/CWC), and (j – l) glaciation ratio only when ice particles and
 827 supercooled liquid water coexist (i.e., IWC/CWC only when both IWC > 0 and LWC > 0). 1-Hz
 828 observations (solid black), 200-s observations (dashed black), 580-s observations (dotted black),
 829 and model simulations (red) are binned at 5°C interval from -40°C to 0°C.



830

831

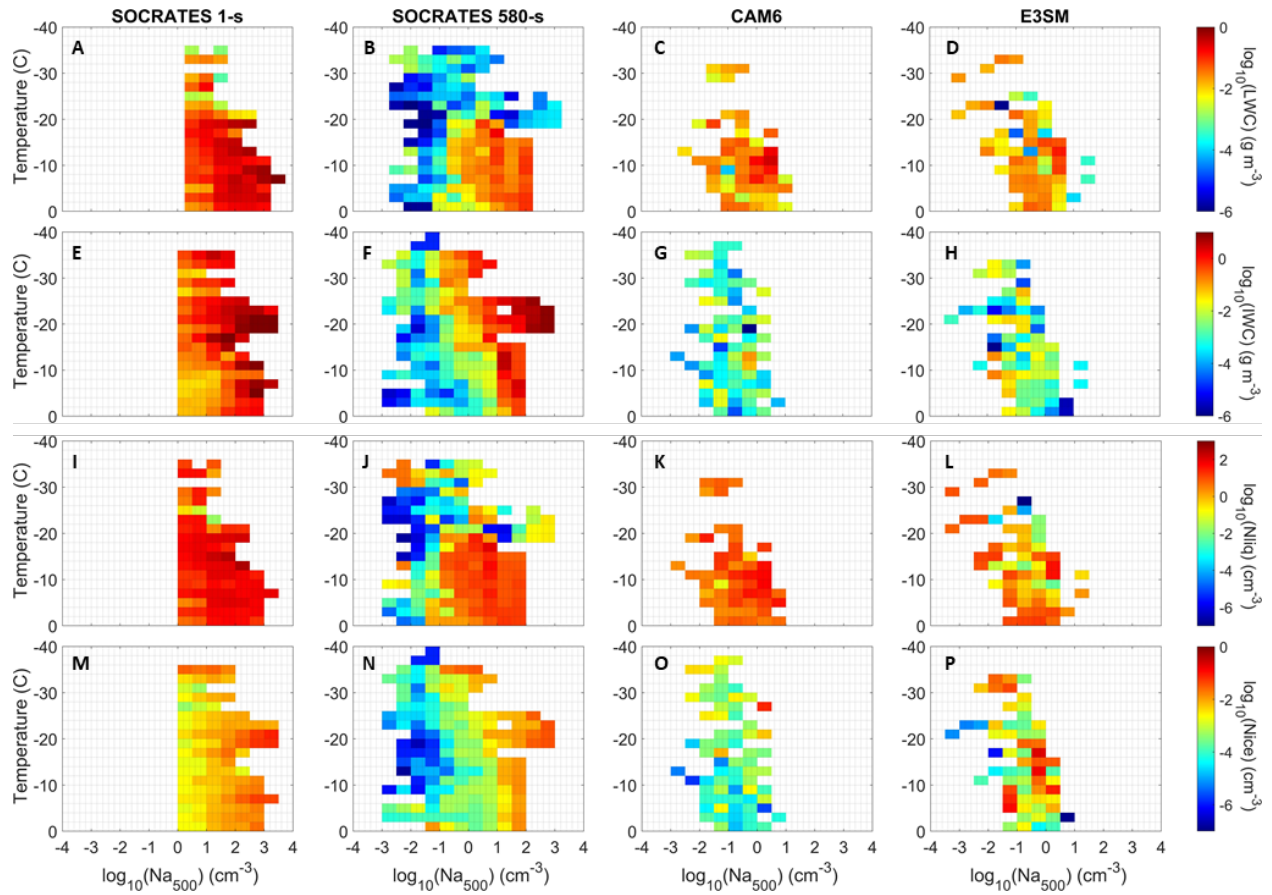
832

833

834

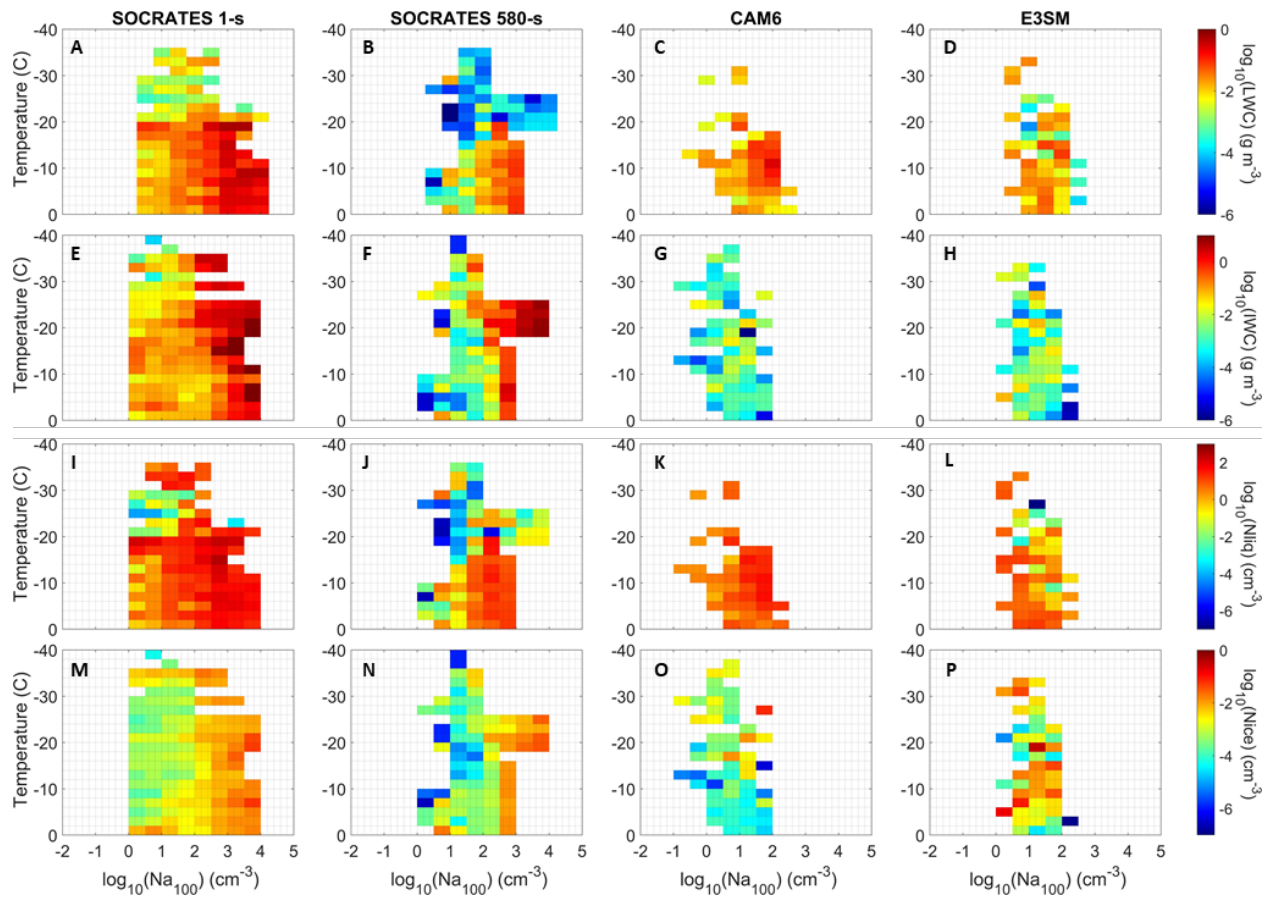
835

Figure 11. PDFs of (a – e) temperature and (f – j) RH_{ice} for all data (solid black line), clear-sky (dashed black), and in-cloud (dotted black) conditions. PDFs of (k – o) temperature and (p – t) RH_{ice} separated into three cloud phases, i.e., ice (blue), mixed (green), and liquid (red) phase. Each PDF is calculated by the number of a certain condition in a bin divided by the total number of samples of that condition of all bins.



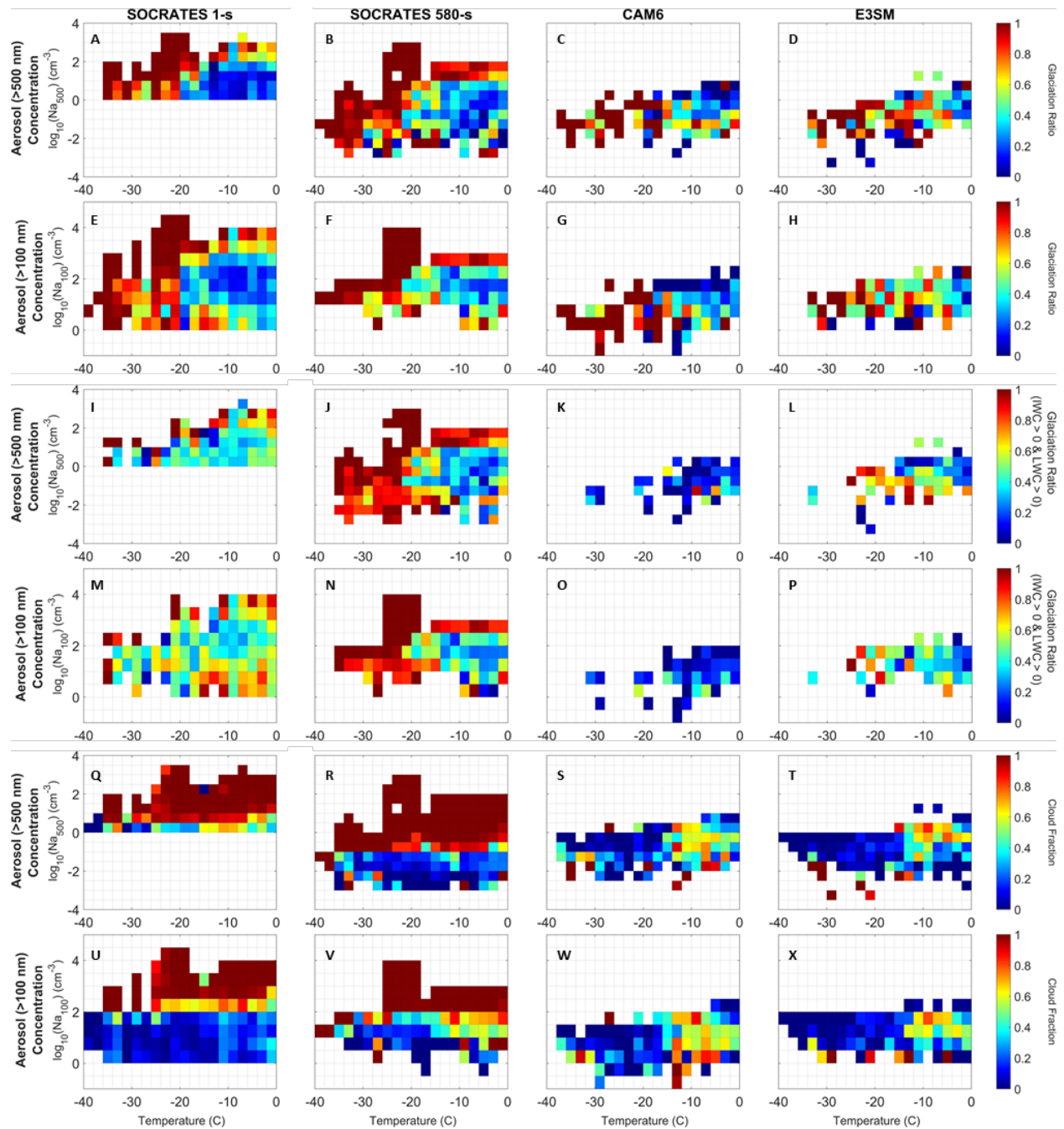
836

837 Figure 12. Cloud microphysical properties with respect to logarithmic scale Na_{500} for 1-s
 838 observations, 580-s averaged observations, CAM6, and E3SM at various temperatures. Bin colors
 839 denote the average of (a – d) $\log_{10}(LWC)$, (e – h) $\log_{10}(IWC)$, (i – l) $\log_{10}(N_{liq})$, and (m – p)
 840 $\log_{10}(N_{ice})$.



841

842 Figure 13. Similar to Figure 12 but for the relationship with $\log_{10}(\text{Na}_{100})$.



843

844 Figure 14. Relationships of (a – h) glaciation ratio of all clouds, (i – p) glaciation ratio only when
 845 ice particles and supercooled liquid water coexist, and (q – x) cloud fraction with respect to (row
 846 1, 3, 5) $\log_{10}(\text{Na}_{500})$ and (row 2, 4, 6) $\log_{10}(\text{Na}_{100})$ at various temperatures. Columns 1 to 4 represent
 847 1-s observations, 580-s observations, CAM6 and E3SM, respectively.